

# Accurate prediction of the solid-state region of the Ni-Al phase diagram including configurational and vibrational entropy and magnetic effects

Wei Shao<sup>a,b</sup>, José Manuel Guevara-Vela<sup>c</sup>, Antonio Fernández-Caballero<sup>d</sup>, Sha Liu<sup>e,\*</sup>,  
Javier LLorca<sup>a,b,\*</sup>

<sup>a</sup> IMDEA Materials Institute, C/Eric Kandel 2, 28906 Getafe, Madrid, Spain

<sup>b</sup> Department of Materials Science. Polytechnic University of Madrid/Universidad Politécnica de Madrid. E. T. S. de Ingenieros de Caminos, 28040 Madrid, Spain

<sup>c</sup> Departamento de Química Física Aplicada, Modulo 14, Universidad Autónoma de Madrid, 28049 Madrid, Spain

<sup>d</sup> Department of Mathematics, Carlos III University of Madrid, Av. de la Universidad, 30, 28911 Leganes, Madrid, Spain

<sup>e</sup> State Key Lab of Metastable Materials Science & Technology, Hebei Key Lab for Optimizing Metal Product Technology and Performance, College of Materials Science & Engineering, Yanshan University, Hebei street 438, Qinhuangdao, 066004, PR China

## ARTICLE INFO

### Keywords:

Al-Ni phase diagram  
Cluster expansion  
Configurational and vibrational entropy  
Magnetic enthalpy

## ABSTRACT

The solid-state region of the Ni-Al phase diagram is predicted from first-principles calculations and Monte Carlo simulations through the cluster expansion formalism. In addition to the formation enthalpy and to the configurational entropy, the vibrational entropy and the magnetic enthalpy are included to calculate the Gibbs free energy of each phase. The computed phase diagram is in excellent agreement with the experimentally accepted phase diagram and provides information about the phase boundary between AlNi<sub>3</sub> and Ni below 300 K. These results demonstrate the potential of this methodology to determine accurately the phase diagram of alloys of technological interest. Finally, the contributions of vibrational entropy and magnetic effects to the overall stability and solubility of the different phases are analyzed independently.

## 1. Introduction

Alloys based on the Ni-Al system are of interest for different engineering applications. Ni-based superalloys present outstanding mechanical properties and high corrosion resistance at high temperature and are widely used in gas-turbine engines for propulsion and energy generation. They contain many elements but are built on the Ni-Al binary system [1] because the main strengthening contribution comes from the dispersion of  $\gamma'$  (AlNi<sub>3</sub>) precipitates. Similarly, addition of small amounts of Ni to Al and Al alloys leads to the formation of diverse Ni-based intermetallic compounds that improve the wear resistance and high temperature strength. Thus Ni-Al alloys are suitable for high temperature structural components as well as for friction and corrosion resistant coatings to protect from aggressive liquids and gasses [2–4]. In addition, intermetallic compounds based on Ni and Al (mainly AlNi<sub>3</sub> and AlNi) present low-density, good thermal conductivity, oxidation resistance and high melting temperature [2] and have applications as coatings and high temperature structural elements when they are alloyed with other elements [5–7] to overcome the brittleness associated with

their ordered lattice structure [8]. Other applications of Ni-Al alloys are found in catalytic devices [9,10] nanotechnology [11], and so on.

Obviously, the Ni-Al phase diagram is a crucial factor to design and improve mechanical and functional properties of alloys based in these chemical elements and different attempts to predict the Ni-Al phase diagrams based in the Calphad method have been reported in the literature [12–16]. They start by discrete thermomechanical and phase equilibria data obtained from experiments and use different approximations (sublattice model [12,16], substitution solution model [13] and order-disorder formalism [15]) to obtain expressions for the free energies of the different phases that rely in fitting parameters that are optimized by comparison with the experimental phase diagrams. More recent calculations [15] also rely in DFT data of the enthalpies of formation but the effect of vibrational entropy is not included. Notwithstanding the success of the Calphad strategy, the good agreement with the experimental phase diagram has to be partially attributed to the fitting strategy and it is doubtful whether the actual values of the free energies for the different intermetallic compounds are accurate outside of the fitting range and can be used, for instance, to predict phase

\* Corresponding authors at: Department of Materials Science. Polytechnic University of Madrid. E. T. S. de Ingenieros de Caminos, 28040 Madrid, Spain and IMDEA Materials Institute, C/Eric Kandel 2, 28906 Getafe, Madrid, Spain; and Yanshan University, Qinhuangdao, 066004, PR China.

E-mail addresses: [shaliu@ysu.edu.cn](mailto:shaliu@ysu.edu.cn) (S. Liu), [javier.llorca@upm.es](mailto:javier.llorca@upm.es), [javier.llorca@imdea.org](mailto:javier.llorca@imdea.org) (J. LLorca).

<https://doi.org/10.1016/j.actamat.2023.118962>

Received 10 February 2023; Received in revised form 20 April 2023; Accepted 24 April 2023

Available online 25 April 2023

1359-6454/© 2023 The Author(s). Published by Elsevier Ltd on behalf of Acta Materialia Inc. This is an open access article under the CC BY license (<http://creativecommons.org/licenses/by/4.0/>).

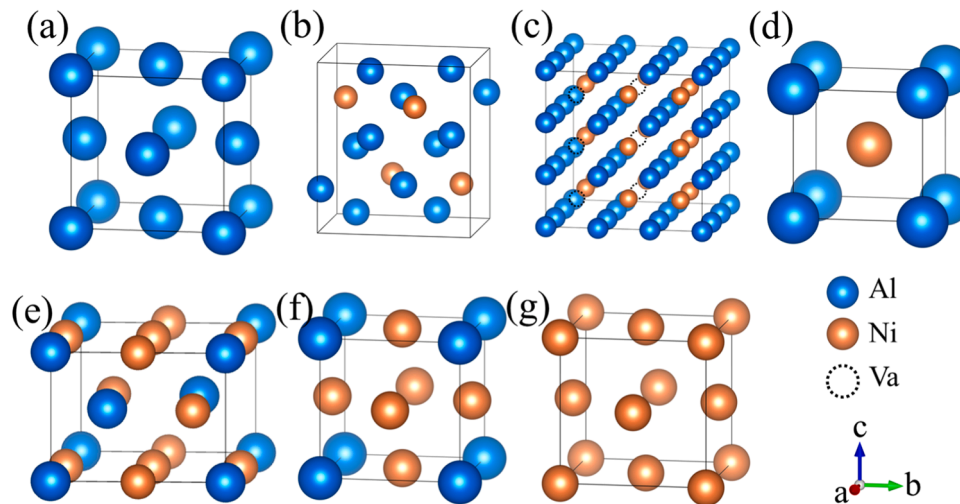


**Fig. 1.** Stable phases in Ni-Al alloys. (a)  $\gamma$ -Al. (b)  $\text{DO}_{11}$ - $\text{Al}_3\text{Ni}$ . (c)  $\text{D}_{513}$ - $\text{Al}_3\text{Ni}_2$ . (d)  $\beta$ -AlNi. (e)  $\delta$ - $\text{Al}_3\text{Ni}_5$ . (f)  $\gamma'$ - $\text{AlNi}_3$ . (g)  $\gamma$ -Ni.

diagrams of ternary systems based on Ni-Al. Moreover, the presence of impurities and the precision of the measurements will affect the phase diagrams [17], and a long annealing time is necessary to reach the stability or to discriminate metastable from stable phases because the convergence towards thermodynamic equilibrium can be hindered by slow kinetics [18,19]. Moreover, there are often regions in the phase diagram in which the experimental information is limited. For instance, the  $\text{Al}_3\text{Ni}_5$  phase has been reported to proceed from a peritectoid reaction between AlNi<sub>3</sub> and AlNi phases but there are some uncertainties about the formation mechanism as well as about the range of Ni solubility in the phase diagram [20–24]. Robertson et al. [21] found that the maximum temperature for stable  $\text{Al}_3\text{Ni}_5$  phase is 973 K and its solubility is (62–69.5) at.% Ni while Li et al. [25] reported that  $\text{Al}_3\text{Ni}_5$  is only stable below 923 K and the solubility range is (54.7–59.4) at.% Ni. Moreover, other researchers considered  $\text{Al}_3\text{Ni}_5$  a line compound [26]. Additionally, two morphologies of  $\text{Al}_3\text{Ni}_5$  have been observed by optical microscopy, namely striped and lath-like, which point out to two different routes to form  $\text{Al}_3\text{Ni}_5$  [27]. One path starts with metastable AlNi ( $\text{Li}_{10}$ ) phase [24] and the other with the stable AlNi ( $\text{B}_2$ ) phase [23]. However, the transformation mechanism for each one is not clear.

With the development of Integrated Computational Materials Engineering (ICME), it is urgent to obtain non-empirical thermodynamic description of the phase diagrams of alloys of huge technological interest (such as the Al-Ni system) that overcome current approaches based on conventional optimization from experimental data. These objectives can be achieved by means of first-principles calculations and statistical mechanics principles supported by the cluster expansion (CE) formalism [28–30]. In this strategy, the mixing enthalpies of different configurations at 0 K are obtained from density functional theory (DFT) calculations and those on the convex hull in the enthalpy-composition space are treated as ground state phases at 0 K. The thermodynamic properties of each phase at different temperatures depends on all the possible microstates whose properties can be easily and accurately determined by means of the CE formalism [28–30]. Thus, Gibbs free energies of different phases including the configurational entropic contribution can be obtained as a function of temperature from Monte Carlo (MC) simulations using the principles of statistical mechanics.

An accurate determination of the phase diagram also requires to include the vibrational entropic contribution to determine the free energy [31,32]. Assuming that the quasi-harmonic approximation holds [33], the thermal properties of solid materials are traced back to those of a phonon system whose frequencies are allowed to depend on the volume. Thus, phonon calculations have to be carried out to determine the force constant matrix of each atom, which reflects the energy response from lattice vibration at each temperature [34]. The lattice vibration is a

degree of freedom under the configurational dimension and its contribution to the free energy should be assessed for all possible microstates but this is not possible because of computational effort required for the phonon calculations [35,36]. This effort can be reduced dramatically in the case of simple lattices if the force constant matrix (which is used to obtain the phonon density of states) is replaced by a diagonal matrix with only two independent terms (stretching and bending stiffness) that can be calculated for each type of bond. This methodology has been successfully used to calculate the vibrational entropy contribution to the free energy of different intermetallic compounds [37–39] and was recently applied to predict the whole phase diagram of the Al-Li system [40]. The calculated phase diagram showed excellent agreement with the Calphad one and pointed out the uncertainties in the miscibility gap between  $\alpha$ -Al and  $\text{Al}_3\text{Li}$ .

A first attempt to predict the Ni-Al phase diagram from first principles calculations was performed by Pasture et al. [41]. Although their predictions were in agreement with experimental data in several points, the accuracy was limited because relaxation and vibrational effects were not taken into account. More recently, Goiri and Van der Ven [42] studied the phase and structural stability of the Ni-Al system, with particular emphasis in the regions where the alloy transitions from fcc to bcc. They confirmed the stability of AlNi and AlNi<sub>3</sub> intermetallic compounds but also showed discrepancies with respect to the experimental data that could be attributed to the vibrational entropic contribution, that was not included in the analysis.

In this investigation, the whole solid-state region of the Ni-Al phase diagram is accurately predicted from first-principles calculations and MC simulations. In addition to the configurational and vibrational entropy, it should be noted that the stable phases (AlNi<sub>3</sub> and Ni) in the Ni-rich part of the Ni-Al phase diagram are ferromagnetic and the contribution of magnetic enthalpy has to be taken into account [43,44]. The magnetic entropy contribution is normally much smaller than the configurational and vibrational ones [45,46] and is neglected. It should be noted that the methodology used in our work only deals with solid phase transitions and the liquidus line (and the phase diagram above the liquidus line) cannot be predicted. Thus, eutectic and peritectic phase transitions are not included in our results. The computed phase diagram is compared with the currently accepted Calphad phase diagram and the contributions of vibrational entropy and magnetic effects to the overall stability and solubility of the different phases are analyzed independently. Thus, the capability of this methodology to predict accurate phase diagrams of alloys of technological interest is clearly established.

**Table 1**

Structural information of the stable phases in the Ni-Al phase diagram.

Composition	Symmetry	Lattice constants (Å)	phase
Al	Fm3m	$a = b = c = 3.48$	$\gamma$
Al <sub>3</sub> Ni	Pnma	$a = 4.77, b = 6.56, c = 7.30$	DO <sub>11</sub>
Al <sub>3</sub> Ni <sub>2</sub>	P3m1	$a = b = 3.99, c = 4.88$	D5 <sub>13</sub>
AlNi	Pm3m	$a = b = c = 2.86$	B <sub>2</sub> ( $\beta$ )
Al <sub>3</sub> Ni <sub>5</sub>	Cmmm	$a = 4.996, b = 4.996, c = 3.740,$ $\alpha = \beta = 90^\circ, \gamma = 97.46^\circ$	$\delta$
AlNi <sub>3</sub>	Pm3m	$a = b = c = 3.52$	L1 <sub>2</sub> ( $\gamma'$ )
Ni	Fm3m	$a = b = c = 3.48$	$\gamma$

## 2. Methodology

### 2.1. Phases in Ni-Al alloys

The stable phases according to the accepted Ni-Al phase diagram are Al, Al<sub>3</sub>Ni, Al<sub>3</sub>Ni<sub>2</sub>, AlNi, Al<sub>3</sub>Ni<sub>5</sub>, AlNi<sub>3</sub> and Ni [2,13]. Their crystal structures are depicted in Fig. 1 and the corresponding structural information is listed in Table 1. Based on our previous experience, some phases with complex structure can be treated as a distorted configuration on a simpler lattice [40]. After careful analysis, it was concluded that all phases in Ni-Al phase diagram – with the exception of Al<sub>3</sub>Ni – can be treated as configurations existing on fcc or bcc lattices, with the atomic sites accommodating Al and Ni atoms. Al<sub>3</sub>Ni<sub>2</sub> can also be treated as a configuration on a bcc lattice, with the Ni sublattice sites of AlNi (which is CsCl type B<sub>2</sub> structure) accommodating Ni atoms and vacancies, while the Al sublattice site of AlNi only accommodates Al atoms. In the case of  $\delta$  – Al<sub>3</sub>Ni<sub>5</sub>, the orthorhombic lattice is slightly distorted and one of the three angles between the principal axes of the lattice is not 90° ( $\gamma = 97.46^\circ$ , Table 1).

### 2.2. DFT calculations

All configurations enumerated by the ATAT code [47] were optimized using first-principles calculations. The electron exchange-correlation was described by the generalized gradient approximation with the Perdew-Burke-Ernzerhof exchange-correlation functional and ultrasoft pseudopotentials, as implemented in Quantum Espresso [48,49]. An energy cutoff of 60 Ry was adopted for the plane-wave expansion of the electronic wave functions. The Brillouin zone was sampled by the Monkhorst-Pack scheme [50] with a k-point density of 40 points/Å<sup>-1</sup>. Two stable phases with ferromagnetism appear in the Ni-Al phase diagram, namely AlNi<sub>3</sub> and Ni, while all other stable phases are nonmagnetic. Therefore, an initial magnetic moment was set to 0.28  $\mu_B$  for Ni atoms, and 0  $\mu_B$  for Al atoms in collinear calculations was included in the simulations for the configurations with >75 at.% Ni [45]. All degrees of freedom of each configuration including volume, shape, and internal atomic positions, were allowed to relax under zero pressure.

### 2.3. Bond length vs. bond stiffness relationship

The bond length vs. bond stiffness (L-S) relationship for each lattice was determined from different configurations. Since this relationship is transferable in configurations within the same lattice [51–53], only four configurations – including the elementary ones – were used. The relaxed configurations were expanded up to 10% in volume in increments of 2%, in order to generate bonds with different lengths. Then, supercells of the expanded configurations were constructed. The supercells of fcc Al and fcc Ni contain 60 atoms, those of bcc Al, bcc Ni, bcc AlNi and fcc AlNi<sub>3</sub> contain 64 atoms and those of bcc Al<sub>3</sub>Ni and fcc Al<sub>3</sub>Ni contain 96 atoms. A displacement of 0.1 Å was applied for each symmetrically different atom within each configuration. Each configuration with different volumes is relaxed using the parameters indicated in Section 2.2.

The force constant matrix  $\Psi_{ij}$  is the second derivative of the energy  $E$

of the deformed supercell with respect to displacements  $u$  [54],

$$\Psi(i,j) = \frac{\partial^2 E}{\partial u_i \partial u_j} \quad (1)$$

where  $u_i$  and  $u_j$  stand for the displacements of atoms  $i$  and  $j$ . For each configuration, the phonon DOS is determined using the Phonopy code [35] from the dynamical matrix  $D_{ij}(q)$ , whose eigenvalues are obtained from the Fourier transform of  $\Psi(i,j)$  at wavevector  $q$  [55].

$\Psi(i,j)$  between pairs of symmetrically different atoms can be simplified to a diagonal matrix with only two independent stiffness terms, namely the stretching stiffness ( $s$ ) and the bending stiffness( $b$ ) [56,57]

$$\Psi(i,j) = \begin{pmatrix} b & 0 & 0 \\ 0 & b & 0 \\ 0 & 0 & s \end{pmatrix} \quad (2)$$

The energy  $E$  in simple lattices, such as fcc and bcc, is mainly related to the interaction between nearest atoms, and only  $\Psi(i,j)$  of the nearest atoms is needed. A L-S relationship for each type of bonding interaction (either Al-Al, Ni-Ni or Al-Ni) was fitted from the values  $b$  and  $s$  obtained for each lattice deformed in tension and compression up to 10% for each configuration.

### 2.4. Vibrational free energy

In the quasi-harmonic approximation, the vibrational entropic contribution to the free energy is determined by Born-von Karman model according to [58]:

$$F_{vib}(V, T) = -TS_{vib}(V, T) \quad (3)$$

where  $T$  is the absolute temperature.  $S_{vib}(V, T)$  is the vibrational entropy at the given temperature and volume that can be expressed as [46]

$$S_{vib}(V, T) = -k_B \int \frac{g(\omega)}{1 - e^{-\frac{\hbar\omega}{k_B T}}} [\theta \log(\theta) + (1 - \theta) \log(1 - \theta)] d\omega \quad (4)$$

where  $\hbar$  is the reduced Planck's constant,  $k_B$  the Boltzmann constant,  $\theta = e^{-\frac{\hbar\omega}{k_B T}}$  and  $g(\omega)$  represents the phonon density of states (DOS), where  $\omega$  denotes the volume-dependent phonon frequencies.

As indicated in Section 2.3, supercell calculations were performed on four different configurations in each lattice in order to obtain the L-S relationships. The  $\Psi(i,j)$  matrices for other configurations in each lattice were obtained directly from the L-S relationships instead of supercell calculations. To this end, all the configurations were initially relaxed to obtain the ideal atomic positions and  $F_{vib}(V, T)$  of each configuration then was obtained from Eqs. (3) and (4).

### 2.5. Temperature-dependent cluster expansion

The temperature-dependent mixing enthalpy  $H_{mix}$  – including the vibrational entropic contribution – of an Al<sub>1-x</sub>Ni<sub>x</sub> configuration (in which all sites accommodate either Al or Ni atoms) in a bcc or fcc lattice can be calculated as [59]

$$H_{mix}^{Al_{1-x}Ni_x}(T) = \left( E_s^{Al_{1-x}Ni_x} - TS_{vib,s}^{Al_{1-x}Ni_x}(T) \right) - (1-x) \left( E_s^{Al} - TS_{vib,s}^{Al}(T) \right) - x \left( E_s^{Ni} - TS_{vib,s}^{Ni}(T) \right) \quad (5)$$

where  $x$  is the atomic fraction of Ni, and  $E_s^{Al_{1-x}Ni_x}$ ,  $E_s^{Al}$  and  $E_s^{Ni}$  stand for the energy of the relaxed Al<sub>1-x</sub>Ni<sub>x</sub>, Al and Ni in the corresponding lattice  $s$ .  $S_{vib,s}^{Al_{1-x}Ni_x}$ ,  $S_{vib,s}^{Al}(T)$  and  $S_{vib,s}^{Ni}(T)$  stand for the vibrational entropy of Al<sub>1-x</sub>Ni<sub>x</sub>, Al and Ni in the corresponding lattice  $s$  at temperature  $T$ .

The temperature-dependent mixing enthalpy of an AlNi<sub>1-y</sub>V<sub>y</sub> configuration (Ni sublattice sites in AlNi can accommodate either Ni atoms or vacancies) in the bcc lattice can be calculated as:

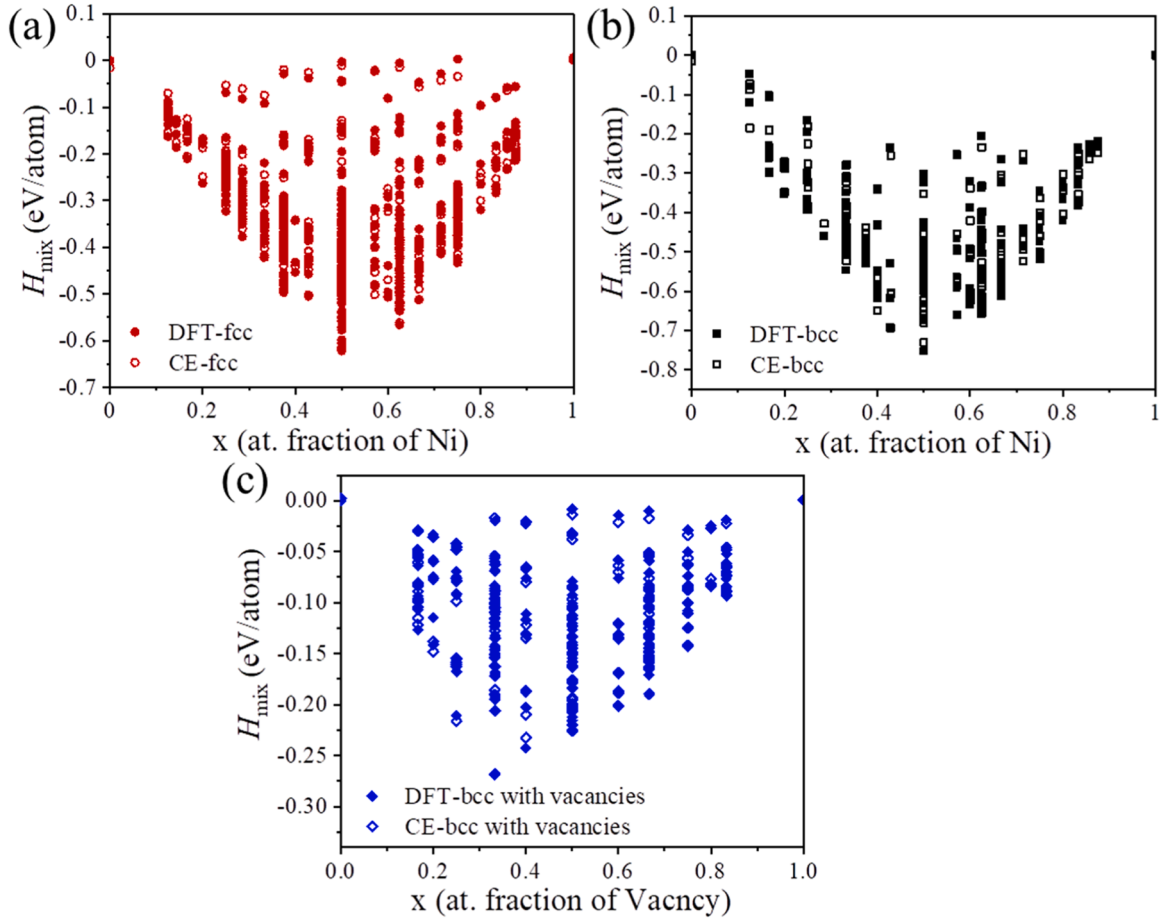


**Fig. 2.** Mixing enthalpy of configurations with different lattice symmetry at 0 K. (a) fcc lattice (b) bcc lattice and (c) bcc lattice with vacancies. The mixing enthalpies calculated by DFT are represented by solid symbols, while the predictions using the CE are represented by open symbols.

$$H_{mix}^{AlNi_{1-y}Va_y}(T) = \left( E_{bcc}^{AlNi_{1-y}Va_y} - TS_{vib,bcc}^{AlNi_{1-y}Va_y}(T) \right) - (1-y) \left( E_{bcc}^{AlNi} - TS_{vib,bcc}^{AlNi}(T) \right) - y \left( E_{bcc}^{AlVa} - TS_{vib,bcc}^{AlVa}(T) \right) \quad (6)$$

where  $y$  is the atomic fraction of vacancy on the Ni sublattice, and  $E_{bcc}^{AlNi_{1-y}Va_y}$ ,  $E_{bcc}^{AlNi}$  and  $E_{bcc}^{AlVa}$  stand for the energy of the relaxed bcc  $AlNi_{1-y}Va_y$ ,  $AlNi$  and  $AlVa$ .  $S_{vib}^{AlNi_{1-y}Va_y}$ ,  $S_{vib,s}^{AlNi}$  and  $S_{vib,s}^{AlVa}$  stand for the vibrational entropy of  $AlNi_{1-y}Va_y$ ,  $AlNi$  and  $AlVa$  in the corresponding bcc lattice at temperature  $T$ . Here we should note that  $AlNi$  and  $AlVa$  are used as the reference systems because of the atomic occupancy of the lattice.

The temperature-dependent CE can be fitted from the temperature-dependent mixing enthalpies of a set of configurations in the same lattice. The CE formalism for a given lattice is expressed as [60,61]

$$H_{mix}(\vec{\sigma}, T) = \sum_{\alpha} m_{\alpha} J_{\alpha}(T) \langle \varphi(\vec{\sigma}) \rangle_{\alpha} \quad (7)$$

where  $\vec{\sigma} = \{\sigma_1, \sigma_2, \dots, \sigma_N\}$  is the vector of occupation variables that indicates which type of atom is found on lattice site  $i$ .  $\sigma_i = -1$  when site  $i$  accommodates an Al atom and  $\sigma_i = +1$  when the site  $i$  accommodates a Ni atom for a lattice without vacancies. For the  $AlNi$  bcc lattice with vacancies, only the Ni sublattice sites have occupation variables:  $\sigma_i = -1$  when site  $i$  accommodates a Ni atom and  $\sigma_i = +1$  when site  $i$  accommodates a vacancy. The summation index in Eq. (7) stands for all distinct clusters  $\alpha$  under symmetry operations of the space group underlying the parent phase.  $m_{\alpha}$  stands for the multiplicity of cluster  $\alpha$  and

$J_{\alpha}(T)$  is the effective cluster interaction (ECI) coefficient of each cluster at temperature  $T$  while  $\langle \varphi(\vec{\sigma}) \rangle_{\alpha}$  is the cluster basis function. The ECIs for each lattice were fitted from the mixing enthalpies by the least squares method, as implemented in the ATAT package. The accuracy of the ECIs was assessed by the cross-validation score as well as by the accurate prediction of the enthalpies of ground state configurations.

It should be noted that the mixing enthalpies given by Eqs. (5) and (6) are the actual formation enthalpies only in the case of the fcc lattice because the stable reference phases are fcc Al and Ni. The temperature-dependent formation enthalpies of the bcc configurations can be obtained from the formation energies and vibrational entropic contribution of the configurations with respect to those of fcc Al and Ni. Moreover, the actual stoichiometry of the configuration should be included in the case of the bcc  $AlNi$  with vacancies. Thus, the temperature-dependent formation enthalpy of bcc configurations,  $H_f$ , can be calculated as:

$$H_f^{Al_{1-x}Ni_x}(T) = \left( E_{bcc}^{Al_{1-x}Ni_x} - TS_{vib,bcc}^{Al_{1-x}Ni_x}(T) \right) - (1-x) \left( E_{fcc}^{Al} - TS_{vib,fcc}^{Al}(T) \right) - x \left( E_{fcc}^{Ni} - TS_{vib,fcc}^{Ni}(T) \right) \quad (8)$$

## 2.6. Phase diagram construction

The grand potential  $\Phi$  is defined as [62]

$$\beta\Phi(\beta, \Delta\mu) = -\ln Z \quad (9)$$

where  $\beta = \frac{1}{k_B T}$  and  $\Delta\mu$  represents the difference in the chemical potential between the components. They are Al and Ni for lattices without va-



cancies, and AlNi and AlVa for bcc lattices with vacancies.  $Z$  stands for the partition function [63], that can be calculated by MC simulations in semi-grand canonical ensemble according to

$$Z = \sum_i \exp(-\beta N(H_f^i - \Delta\mu x)) \quad (10)$$

where  $N$  is the number of sites in the crystal lattice,  $H_f^i$  the formation enthalpy of each possible microstate  $i$  and  $x$  the fraction of one component (namely Ni in fcc and bcc lattices without vacancies and AlVa in bcc lattices with vacancies).

The semi-grand canonical MC simulations of bcc and fcc lattices as well as of bcc lattices with vacancies were performed using the ATAT package.  $20 \times 20 \times 20$  supercells were used for each ground state phase. The fitted CE of each lattice was used to predict  $H_f^i$  from  $H_{mix}^i$ , Eqs. (6) and (8). MC simulations were performed at different  $T$  (from 10 K up to 1800 K) with a temperature increment of 10 K for each chemical potential and within a given range of  $\Delta\mu$  for each phase with increments of 0.005 eV/component in the chemical potential for each temperature. For each value of  $T$  and  $\Delta\mu$ , a MC simulation included 2000 passes for equilibrium, followed by 5000 passes for calculating the thermodynamic averages

From Eqs. (9) and (10), the derivative of the grand potential for each phase can be written as:

$$d(\beta\phi) = N(\langle H_f \rangle - \Delta\mu x)d\beta - N\beta x d(\Delta\mu) \quad (11)$$

where  $\langle H_f \rangle$  stands for the average formation enthalpy.

For a given  $\Delta\mu$ ,  $\phi$  can be calculated as [63]:

$$\phi(\beta_1, \Delta\mu) = \phi(\beta_0, \Delta\mu) + \frac{N}{\beta} \int_{\beta_0}^{\beta_1} (H_f - \Delta\mu x) d\beta \quad (12)$$

and for a given  $\beta$ ,  $\phi$  can be calculated as:

$$\phi(\beta, \Delta\mu_1) = \phi(\beta, \Delta\mu_0) - N \int_{\Delta\mu_0}^{\Delta\mu_1} x d\Delta\mu. \quad (13)$$

The difference between Gibbs and Helmholtz free energies can be neglected during solid-state transformations, so the Gibbs free energy  $G$  is expressed as [64]

$$G = \phi + \Delta\mu x \quad (14)$$

The two-phase boundary between phases that share the same lattice can be determined by the intersection of  $\phi$  obtained from increasing and decreasing  $\Delta\mu$ . For two adjacent phases with different lattice structures, the two-phase equilibrium region in the phase diagram can be determined by the common tangent of their Gibbs free energies curves at a given temperature.

### 3. Temperature-dependent cluster expansion

#### 3.1. Ground state phases

631 configurations with the fcc lattice, 437 configurations with the bcc lattice and 167 configurations with the bcc lattice with vacancies were fully relaxed at zero pressure using Quantum Espresso. The lattice distortion after relaxation was determined to assess whether the lattice symmetry changed. Only configurations whose distortion was below 10% were considered to keep the original lattice symmetry and used to fit the CE for each lattice, following the criteria in the literature [65,66]. Thus, the mixing enthalpies were calculated for 485 fcc configurations and 170 bcc configurations, following Eq. (5), and for 163 bcc configurations with vacancies following Eq. (6). They are plotted with solid symbols in Fig. 2(a), 2(b) and 2(c), respectively.

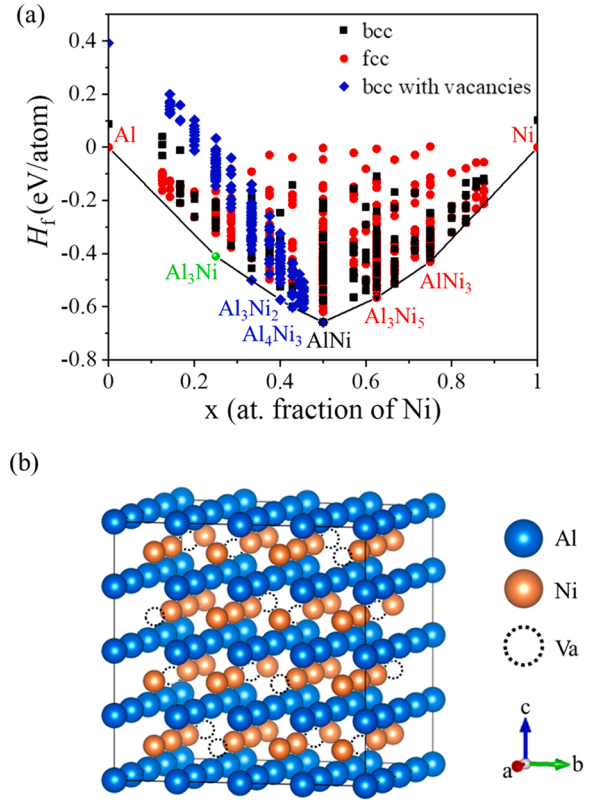


**Fig. 3.** (a) Formation enthalpies of all configurations at 0 K. The ground state phases in the convex hull are connected by the black line.  $\text{Al}_3\text{Ni}$  is neither in the bcc nor the fcc lattice, so it is depicted with a green point. Thus, the ground state phases are Al,  $\text{Al}_3\text{Ni}$ ,  $\text{Al}_3\text{Ni}_2$ ,  $\text{Al}_4\text{Ni}_3$ , AlNi,  $\text{Al}_3\text{Ni}_5$ ,  $\text{AlNi}_3$  and Ni, respectively. (b) Crystal structure of the predicted ground state phase  $\text{Al}_4\text{Ni}_3$ .

The optimized ECIs were obtained for each lattice. Those for the fcc lattice include 25 pair cluster interactions, 20 triplet cluster interactions and 35 quadruplet cluster interactions. The optimized ECIs for the bcc lattice include 1 empty cluster interaction, 1 point cluster interaction, 12 pair cluster interactions, 17 triplet cluster interactions and 7 quadruplet cluster interactions. Finally, the optimized ECIs for the bcc lattice with vacancies include 11 pair cluster interactions, 21 triplet cluster interactions and 12 quadruplet cluster interactions. The values of the ECI at 0 K are depicted in Tables SI, Table SII and Table SIII in the Supplementary Material. The mixing enthalpies for each lattice calculated with the CE formalism are plotted with open symbols in Figs. 2(a) to 2(c). They were in good agreement with the DFT results and the cross-validation scores of the CE predictions were 0.0125 eV/atom, 0.0184 eV/atom and 0.0126 eV/atom for the fcc, bcc and bcc with vacancies configurations, respectively.

The formation enthalpies at 0 K of all configurations (that are equal to the mixing enthalpies for the fcc lattice and are calculated from Eq. (8) for the bcc lattices) are plotted in Fig. 3. The formation enthalpy of  $\text{Al}_3\text{Ni}$  is also included with a green symbol in this figure. The primitive cell of the orthorhombic  $\text{Al}_3\text{Ni}$  phase contains 16 atoms, and the computational work to fit the CE for this lattice will be huge. This effort is not justified because the configurational entropy of this phase with low symmetry is very limited [67]. Thus,  $\text{Al}_3\text{Ni}$  is assumed to be a line compound and corresponding configurational entropy is neglected. The Gibbs free energy of  $\text{Al}_3\text{Ni}$  at different temperatures is replaced by corresponding formation enthalpy at the same temperature, including the vibrational entropic contribution. The ground state phases in the convex hull are connected by the black line in Fig. 3(a). They are Al,  $\text{Al}_3\text{Ni}$ ,  $\text{Al}_3\text{Ni}_2$ ,  $\text{Al}_4\text{Ni}_3$ , AlNi,  $\text{Al}_3\text{Ni}_5$ ,  $\text{AlNi}_3$  and Ni. All of them were included in the majority of experimental and Calphad-based Ni-Al phase

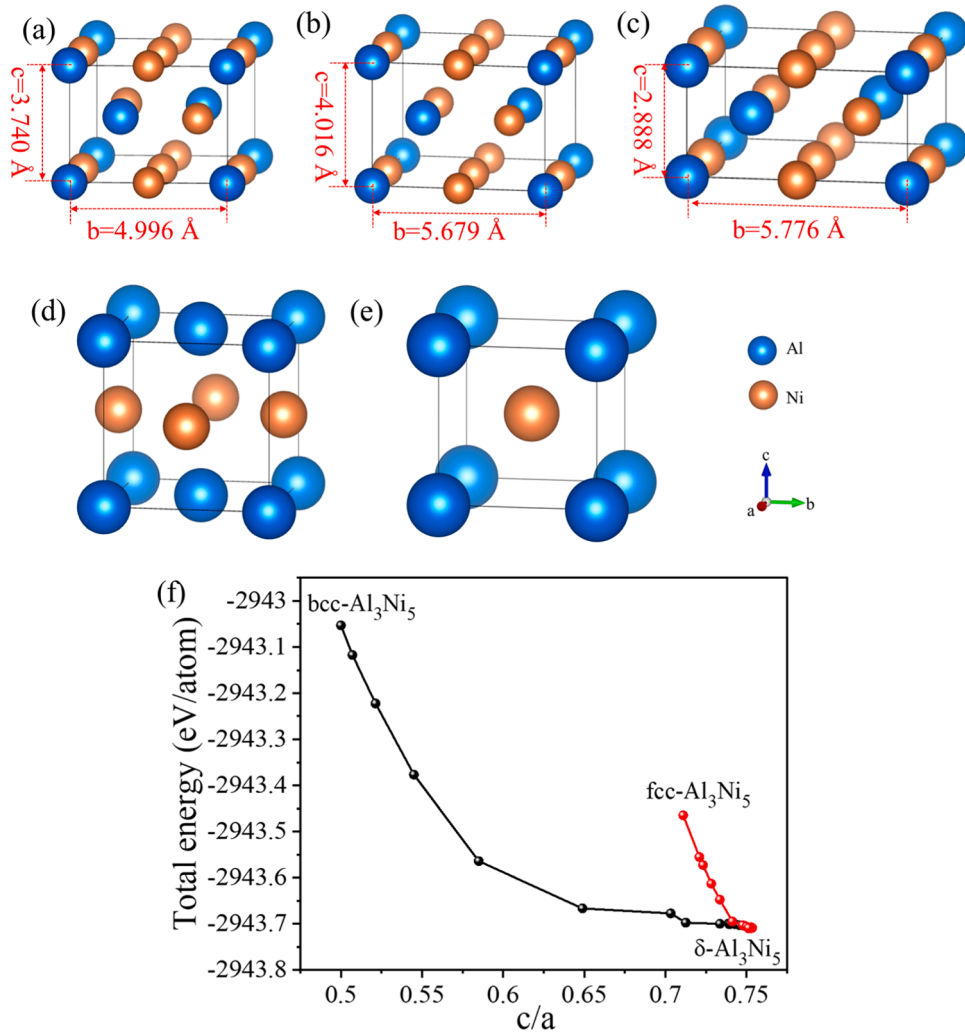


**Fig. 4.** Crystal structures of (a)  $\delta$ -Al<sub>3</sub>Ni<sub>5</sub>, (b) fcc Al<sub>3</sub>Ni<sub>5</sub>, (c) bcc Al<sub>3</sub>Ni<sub>5</sub>, (d) L1<sub>0</sub> (NiAl) martensite, (e) B<sub>2</sub> (NiAl). (f) Transformation path (marked by the change in  $c/a$  ratio) from bcc-Al<sub>3</sub>Ni<sub>5</sub> and fcc-Al<sub>3</sub>Ni<sub>5</sub> to  $\delta$ -Al<sub>3</sub>Ni<sub>5</sub>.

diagrams, with the exception of Al<sub>4</sub>Ni<sub>3</sub>, which is an ordered configuration in the bcc lattice with vacancies, whose structure is displayed in Fig. 3(b). All vacancies appeared at the Ni sublattice and are arranged so that only one site was occupied by a vacancy in any row of the Ni sublattice along of  $x$ ,  $y$ , or  $z$  directions. However, Al<sub>4</sub>Ni<sub>3</sub> has been experimentally reported in several investigations [68–70] with the structure indicated in Fig. 3(b). In addition, it should be noted that different configurations with energies very close to the convex hull (just a few meV/atom) were found for Ni contents between 0.65 and 0.9, in agreement with previous calculations [42].

The DFT calculations showed that two configurations enumerated in fcc and bcc lattices (depicted in Figs. 4(b) and 4(c), respectively) relaxed into the  $\delta$ -Al<sub>3</sub>Ni<sub>5</sub> phase (Fig. 4(a)). The energy variation during relaxation shown in Fig. 4(f) reveals that the bcc and fcc Al<sub>3</sub>Ni<sub>5</sub> configurations do not coincide with any local minima and will spontaneously collapse to  $\delta$ -Al<sub>3</sub>Ni<sub>5</sub>. According to the literature [71], two different routes for the formation of Al<sub>3</sub>Ni<sub>5</sub> have been observed: one starts from the L1<sub>0</sub> (NiAl) martensite in the fcc lattice (Fig. 4(d)) and the other from the B<sub>2</sub> (NiAl) in the bcc lattice (Fig. 4(e)). Moreover, the formation of Al<sub>3</sub>Ni<sub>5</sub> appears to be diffusion-controlled [22]. The transformation from L1<sub>0</sub> martensite (Fig. 4(d)) to fcc Al<sub>3</sub>Ni<sub>5</sub> (Fig. 4(b)) only needs short-range diffusion of the Ni atoms in the Al sublattice and leads to small changes in the  $c/a$  ratio (from 0.711 in L1<sub>0</sub> to 0.749 in fcc Al<sub>3</sub>Ni<sub>5</sub>). The transformation from B<sub>2</sub> (AlNi) (Fig. 4(e)) to bcc Al<sub>3</sub>Ni<sub>5</sub> (Fig. 4(c)) involves atomic diffusion plus a Bain-type distortion [23,

72–74] to change the  $c/a$  ratio from 0.5 in B<sub>2</sub> (AlNi) to 0.749 in bcc Al<sub>3</sub>Ni<sub>5</sub>. Afterwards, both fcc and bcc Al<sub>3</sub>Ni<sub>5</sub> will collapse to  $\delta$ -Al<sub>3</sub>Ni<sub>5</sub> by adjusting the crystal shape ( $\gamma$  from 90° to 97.46°), which is shear controlled. However, the transformation path from L1<sub>0</sub> martensite has a steeper slope (Fig. 4(e)) and the changes in the lattice parameters from L1<sub>0</sub> to  $\delta$ -Al<sub>3</sub>Ni<sub>5</sub> (Fig. 4(b) to (a)) are smaller than from B<sub>2</sub> to  $\delta$ -Al<sub>3</sub>Ni<sub>5</sub> (Fig. 4(c) to (a)). So, Al<sub>3</sub>Ni<sub>5</sub> is treated as a fcc configuration.

### 3.2. Bond length vs. bond stiffness relationship

There are three types of chemical bonds between different species in Ni-Al alloys, namely Al-Al, Ni-Ni and Al-Ni bonds. Their  $L$ - $S$  relationships in the bcc lattice were obtained from four ordered configurations Al, AlNi, Al<sub>5</sub>Ni and Ni, whose structures are shown in Fig. 5. The nearest-neighbor (NN) bonds in each lattice are the ones that contribute most to the vibrational free energy [57,75,76], so only the NN bonds were considered. The NN bonds in bcc Al (Fig. 5(a)) and bcc Ni (Fig. 5(d)) are Al-Al and Ni-Ni, and their equilibrium bond lengths are 2.782 Å and 2.387 Å, respectively. The NN bonds in bcc AlNi (Fig. 5(b)) are Al-Al, Ni-Ni and Al-Ni, and the respective equilibrium bond lengths are 2.481 Å, 2.864 Å and 2.864 Å. The NN bonds in bcc Al<sub>5</sub>Ni (Fig. 5(c)) are two kinds of Al-Al (equilibrium bond lengths of 2.850 Å and 2.778 Å), Ni-Ni (equilibrium bond length is 2.778 Å) and Al-Ni (equilibrium bond length is 2.464 Å).

The ordered bcc Ni-Al configurations were expanded to different

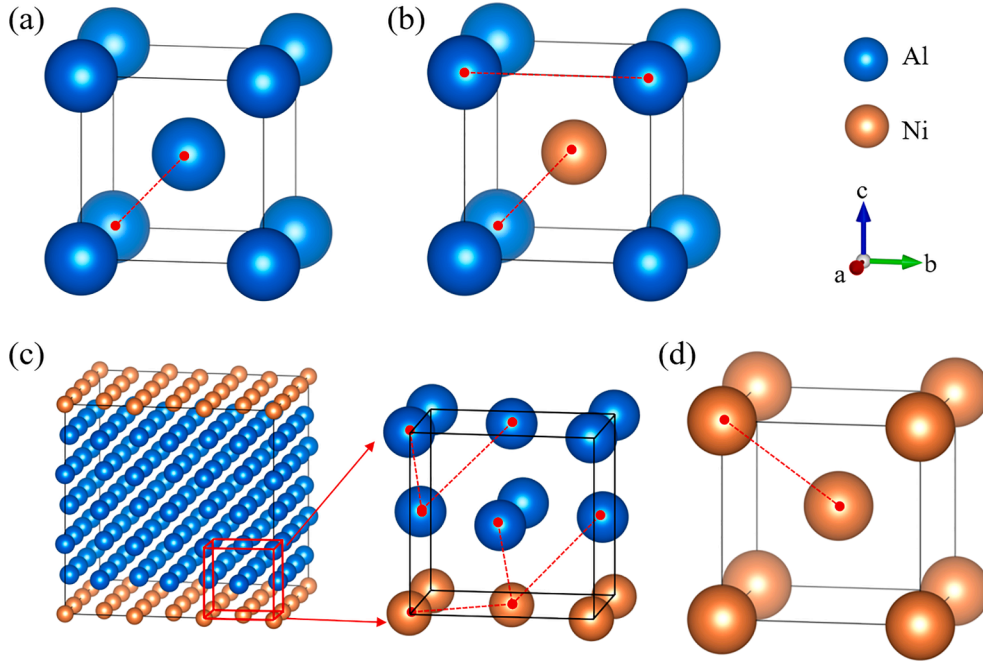


Fig. 5. Crystal structures of ordered bcc Ni-Al configurations. (a) Al. (b) AlNi. (c) Al<sub>5</sub>Ni. (d) Ni. The NN bonds in each crystal structure are indicated by red lines.

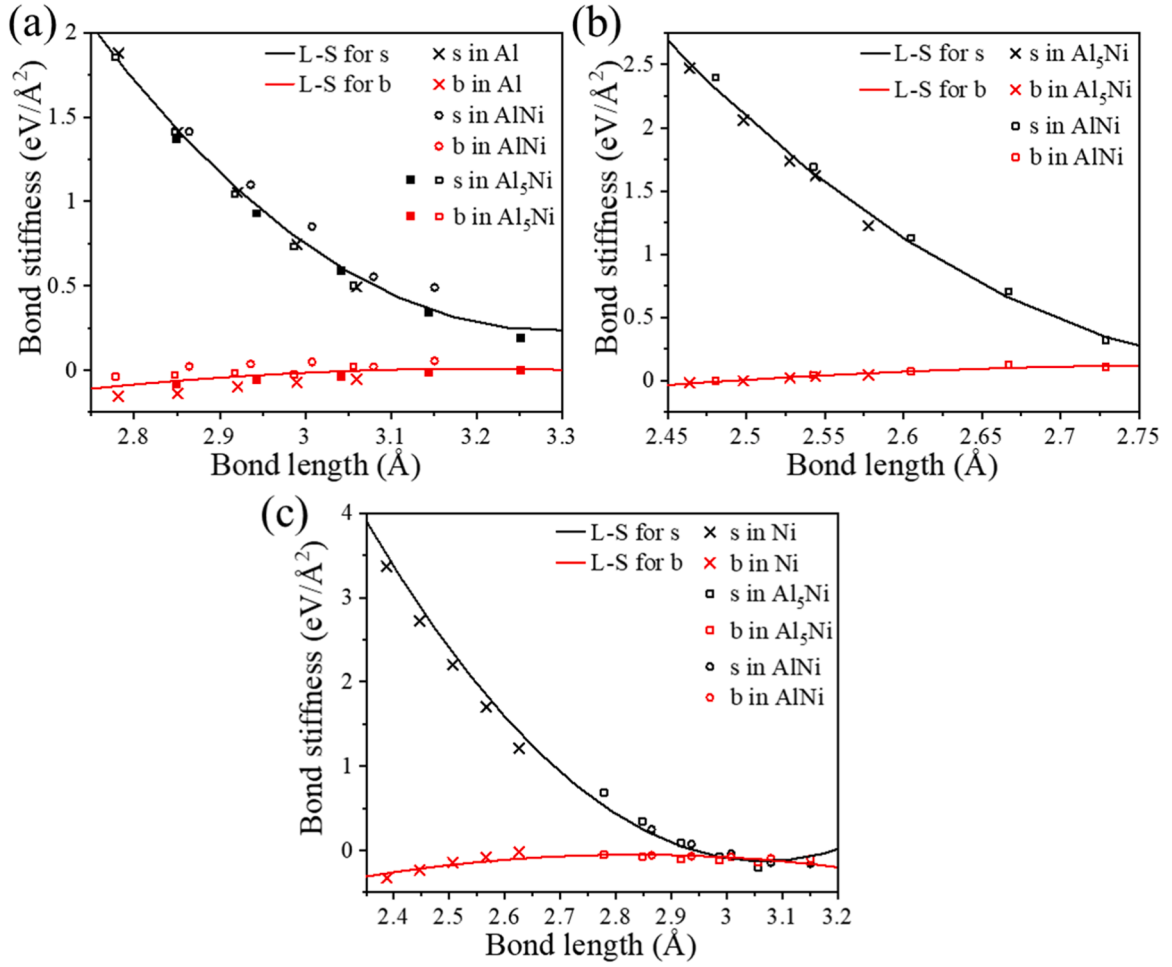


Fig. 6. Bond length vs. bond stiffness relationships in the bcc lattice. (a) Al-Al bond. (b) Al-Ni bond. (c) Ni-Ni bond. The symbols stand for the results obtained from ordered bcc Ni-Al configurations by full phonon calculations according to Eqs. (1) and (2). The black and red curves stand for the fitted quadratic polynomials.

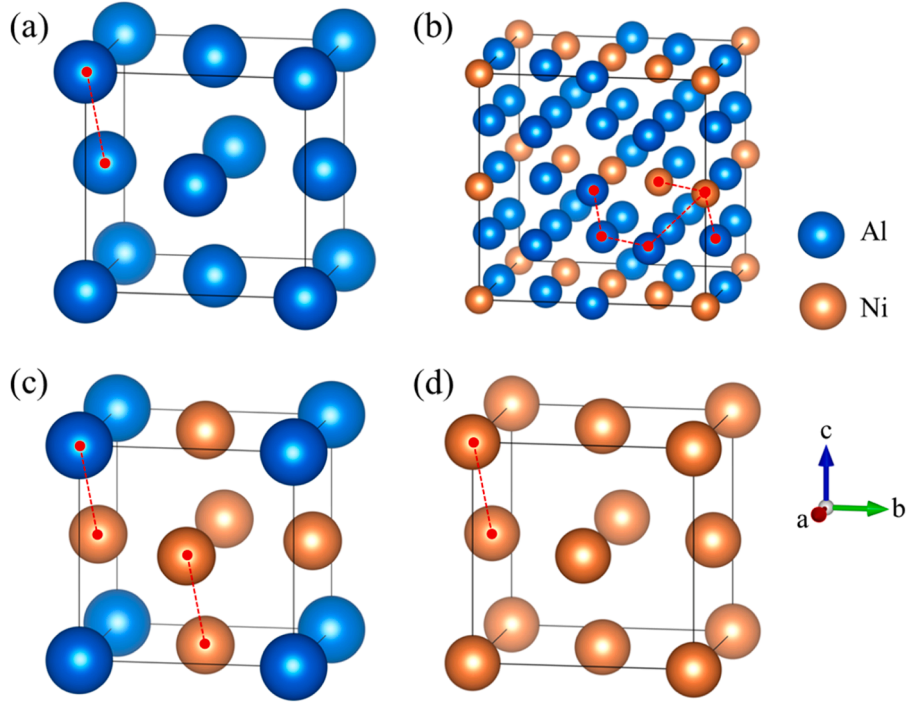


Fig. 7. Crystal structures of ordered fcc Ni-Al configurations. (a) Al. (b)  $\text{Al}_3\text{Ni}$ . (c)  $\text{AlNi}_3$ . (d) Ni. The NN bonds in each crystal structure are indicated by red lines.

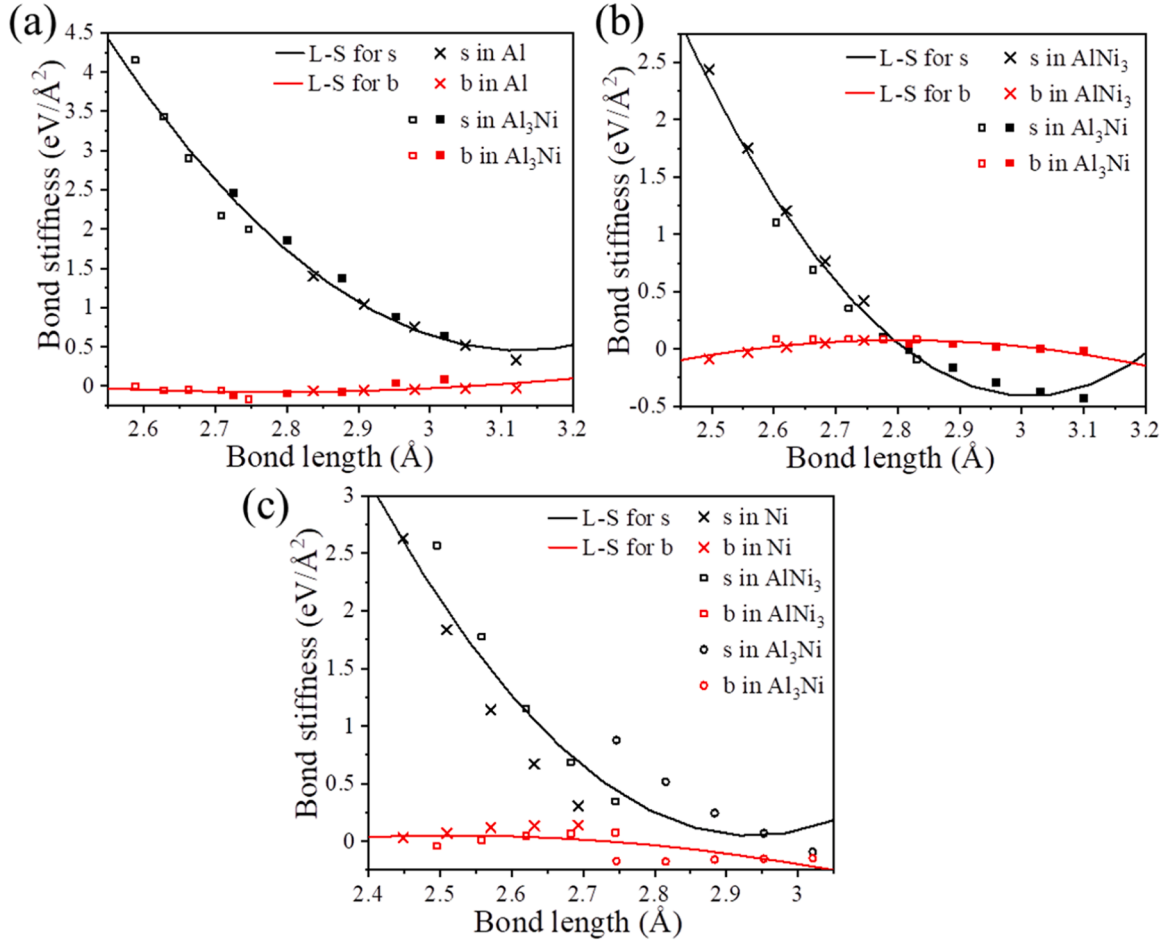
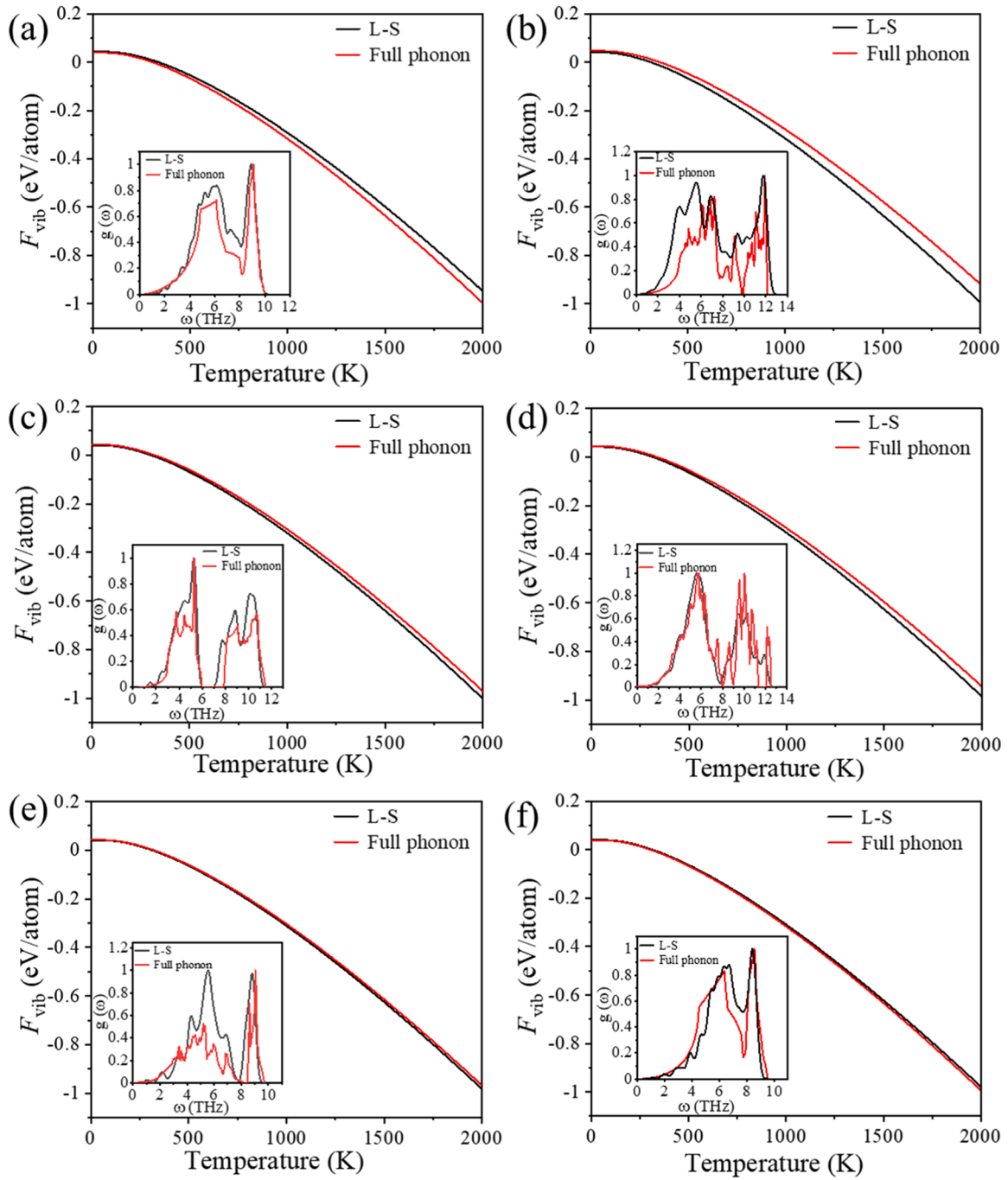


Fig. 8. Bond length vs. bond stiffness relationships in fcc lattice. (a) Al-Al bond. (b) Al-Ni bond. (c) Ni-Ni bond. The symbols stand for the results obtained from ordered fcc Ni-Al configurations by full phonon calculations according to Eqs. (1) and (2). The black and red curves are the fitted quadratic polynomials.





**Fig. 9.** Vibrational free energies of the different stable phases in the Ni-Al system obtained from full phonon calculations (red lines) and from the L-S relationships (black lines). (a)  $\gamma$ -Al. (b)  $D513\text{-Al}_3\text{Ni}_2$ . (c)  $B_2(\beta)\text{-AlNi}$ . (d)  $\delta\text{-Al}_3\text{Ni}_5$ . (e)  $\gamma'\text{-AlNi}_3$ . (f)  $\gamma\text{-Ni}$ . The DOS predicted for each phase using both strategies is plotted in the inset of each figure.

volumes and the force constant matrices of Al-Al, Ni-Ni and Al-Ni bonds in different volumes were determined from full phonon calculations. The stretching and bending stiffnesses of each bond as a function of the bond length are depicted with different symbols in Fig. 6. The stretching stiffness of the three bonds decrease as bond length increases, while the bending stiffness increases slightly. The L-S relationships of stretching and bending stiffness for each chemical bond were fitted with quadratic polynomials using the least-squares method. They are represented by the black and red curves in Fig. 6. It is obvious that the L-S relationship for a given chemical bond holds the same trend in different configurations and, thus, the force constant matrix is transferable to different configurations in the bcc lattice.

The L-S relationships of Al-Al, Ni-Ni and Al-Ni bonds in the fcc lattice were obtained from four ordered configurations, namely Al,  $\text{Al}_3\text{Ni}$ ,  $\text{AlNi}_3$  and Ni, whose structures are shown in Fig. 7. The NN bonds in fcc Al and Ni are Al-Al and Ni-Ni (Figs. 7(a) and (d)) and their equilibrium bond lengths are 2.837 Å and 2.448 Å, respectively. The NN bonds in fcc  $\text{AlNi}_3$  (Fig. 7(c)) are Al-Al and Al-Ni, whose equilibrium bond lengths are both 2.495 Å. The NN bonds in fcc  $\text{Al}_3\text{Ni}$  (Fig. 7(b)) are two kinds of Al-Al (whose equilibrium bond lengths are 2.588 Å and 2.726 Å), two kinds of Al-Ni (whose equilibrium bond lengths are 2.604 Å and 2.819 Å) and Ni-Ni (whose equilibrium bond length is 2.746 Å).

The ordered fcc Ni-Al configurations were expanded to different volumes and the force constant matrix of Al-Al, Ni-Ni and Al-Ni bonds in

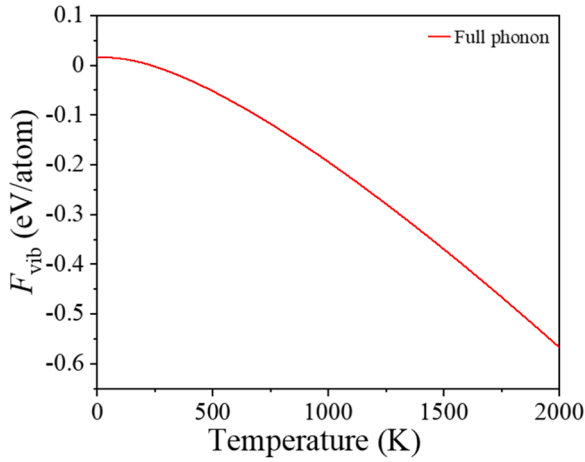


Fig. 10. Vibrational free energy of  $\text{Al}_3\text{Ni}$  obtained by full phonon calculations.

different volumes were determined by full phonon calculations. The stretching and bending stiffnesses of each bond as a function of the bond length are depicted with different symbols in Fig. 8, and they show similar trends to those in Fig. 6. The  $\text{L-S}$  relationships of stretching and bending stiffness of each chemical bond were fitted into quadratic polynomials using the least-squares method, and the represented by the black and red curves in Fig. 8.

It should be noted that equivalent simulations were carried out assuming the Ni is non-magnetic. The  $\text{L-S}$  relationships fitted under this

assumption are depicted in Fig. SI in the Supplementary Materials. The values of the stretching and bending stiffnesses of the non-magnetic configurations were very close to those obtained with magnetism, and it was concluded that the same  $\text{L-S}$  relationship can be used for magnetic and non-magnetic configurations.

### 3.3. Vibrational free energy

The quadratic polynomials in Figs. 6 and 8 can be used to predict the force constant matrix of any bcc and fcc configuration, and as a result, the corresponding vibrational free energy can be obtained through the integration of the phonon DOS through Eqs. (3) and (4). The accuracy of the fitted  $\text{L-S}$  relationships can be assessed by comparison with the results obtained from full phonon calculations on the most relevant phases of the Ni-Al system. The phonon DOS of Al,  $\text{Al}_3\text{Ni}_2$ ,  $\text{AlNi}$ ,  $\text{Al}_3\text{Ni}_5$ ,  $\text{AlNi}_3$  and Ni phases obtained from the  $\text{L-S}$  relationships (black lines) and from full phonon calculations (red lines) are plotted in Fig. 9, together with the vibrational free energies,  $F_{\text{vib}}$ , obtained as a function of temperature. The phonon DOS and vibrational free energies predicted by the  $\text{L-S}$  relationships are consistent with those obtained from full phonon calculations, including in the case of configurations with vacancies, such as  $\text{Al}_3\text{Ni}_2$ . It should be noted that  $\text{Al}_3\text{Ni}$  is not included in Fig. 9 because it has an orthorhombic structure and the corresponding  $\text{L-S}$  relationship was not calculated. The phonon DOS and vibrational free energy of this phase as a function of temperature was only determined from full phonon calculations and it is plotted in Fig. 10. Additionally, the vibrational free energies of ferromagnetic Ni and  $\text{AlNi}_3$  are also compared with those of non-magnetic Ni and  $\text{AlNi}_3$  in Fig. SII in the

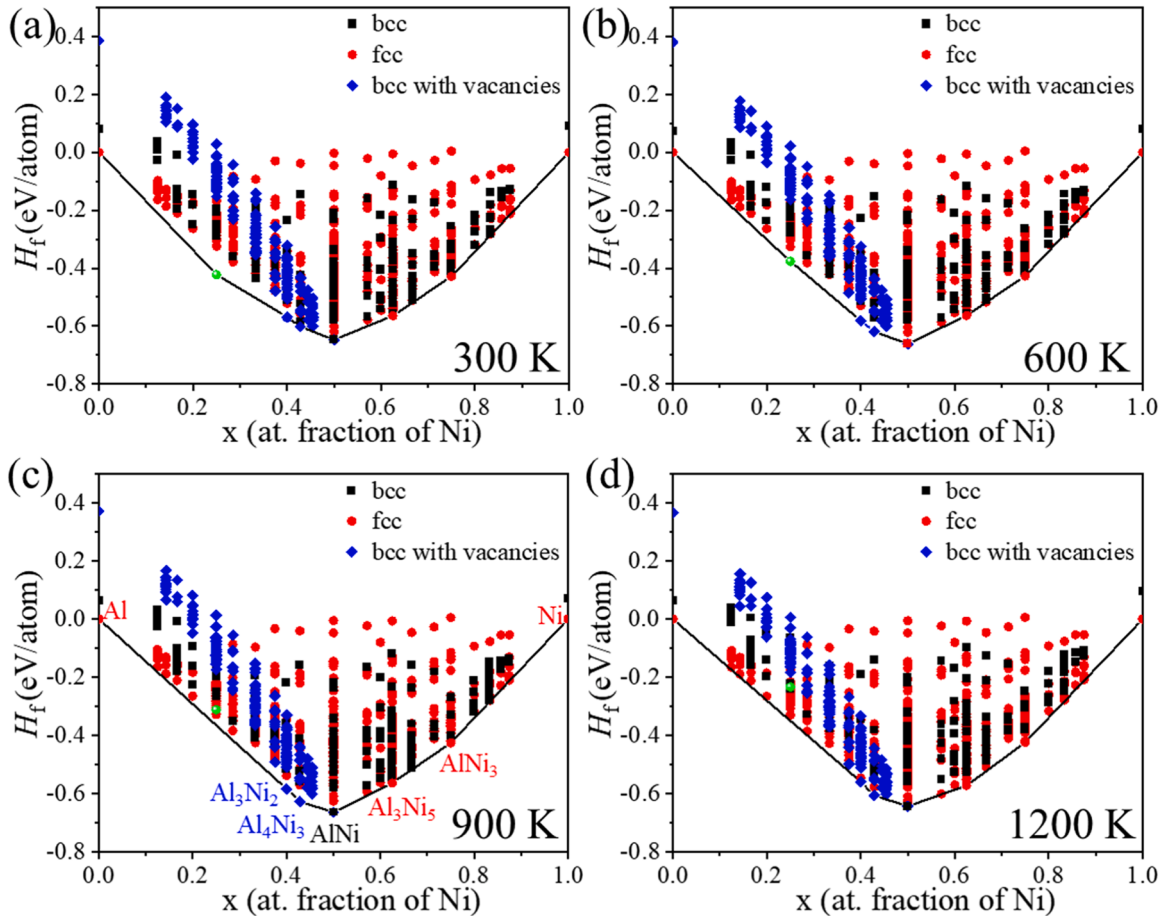


Fig. 11. Formation enthalpies of all configurations in the Ni-Al system at different temperatures. (a) 300 K. (b) 600 K. (c) 900 K. (d) 1200 K. The red symbols stand for the fcc configurations, the black symbols for the bcc configurations, and the blue symbols for the bcc configurations with vacancies. The green symbol stands for  $\text{Al}_3\text{Ni}$ .

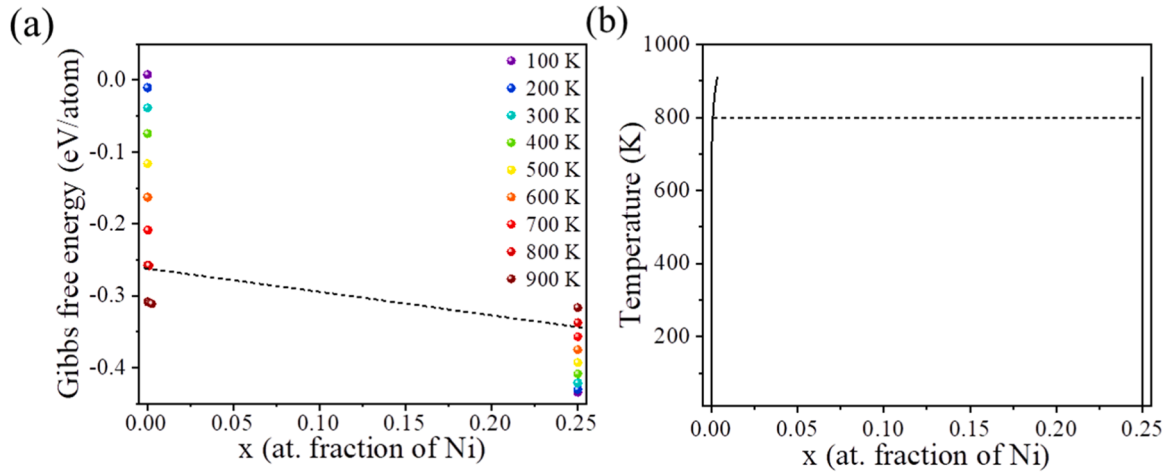


Fig. 12. (a) Gibbs free energies of Al and Al<sub>3</sub>Ni at different temperatures. (b) Phase boundary between Al and Al<sub>3</sub>Ni.

Supplementary Materials. They are superposed, indicating the effect of magnetism on vibrational entropy can be neglected.

### 3.4. Temperature-dependent cluster expansions

The temperature-dependent ECI of the cluster interactions used in Section 3.1 for each lattice were fitted based on the vibrational free energy of the configurations. The temperature-dependent ECI coefficients for fcc lattice, bcc lattice and bcc lattice with vacancies are listed in Tables SI, Table SII and Table SIII in the Supplementary Materials. The formation enthalpies at different temperatures (300 K, 600 K, 900 K and 1200 K) of all configurations in the three lattices are plotted in Fig. 11. They were obtained from the DFT simulations of the formation energy plus the vibrational entropic contribution obtained from the I-S relationships. They are compared with the formation enthalpies predicted by the temperature-dependent CEs in Fig. SIII, Fig. SIV and Fig. SV in the Supplementary Materials. Both were in good agreement and the corresponding cross-validation scores were similar to those obtained for the CE at 0 K.

The formation enthalpies in Fig. 11 include the contribution of formation enthalpy at 0 K and the vibrational entropy at different temperatures. Thus, the convex hulls at different temperatures provide information about the stability change of each phase due to lattice vibration. The phases on the convex hulls at 300 K (Fig. 11(a)) and 600 K (Fig. 11(b)) are the same as at 0 K (Fig. 3(a)). Nevertheless, Al<sub>3</sub>Ni

(marked with a green symbol) is no longer located in the convex hull at 900 K (Fig. 11(c)), and this change is due to the vibrational entropy. The vibrational free energy of Al<sub>3</sub>Ni is displayed in Fig. 10 as a function of temperature. The reduction in the vibrational free energy of Al<sub>3</sub>Ni with temperature is much smaller than that found for all other stable phases in Fig. 9, leading to the instability of this phase at high temperature. Other phases including Al, Al<sub>3</sub>Ni<sub>2</sub>, Al<sub>4</sub>Ni<sub>3</sub>, AlNi, Al<sub>3</sub>Ni<sub>5</sub>, AlNi<sub>3</sub> and Ni are always on the convex hull.

## 4. Phase diagram construction

### 4.1. Al-Al<sub>3</sub>Ni phase boundary

Semi-grand canonical MC simulations were performed from each ground state phase. In the Al-rich solid region of the phase diagram, the adjacent phase to fcc Al is Al<sub>3</sub>Ni, which has an orthorhombic lattice. Therefore, the solid phase boundary between Al and Al<sub>3</sub>Ni can only be determined by the common tangent of their Gibbs free energies. The Gibbs free energy of Al was calculated from Eq. (14), the Gibbs free energy of Al<sub>3</sub>Ni at different temperatures was replaced by the formation enthalpy at different temperatures because it is a line compound. The dash line in Fig. 12(a) shows the common tangent at 800 K, from which the composition of each phase at this temperature is determined. This strategy was used to obtain the two-phase region between Al and Al<sub>3</sub>Ni in Fig. 12(b). There is no common tangent between both phases,

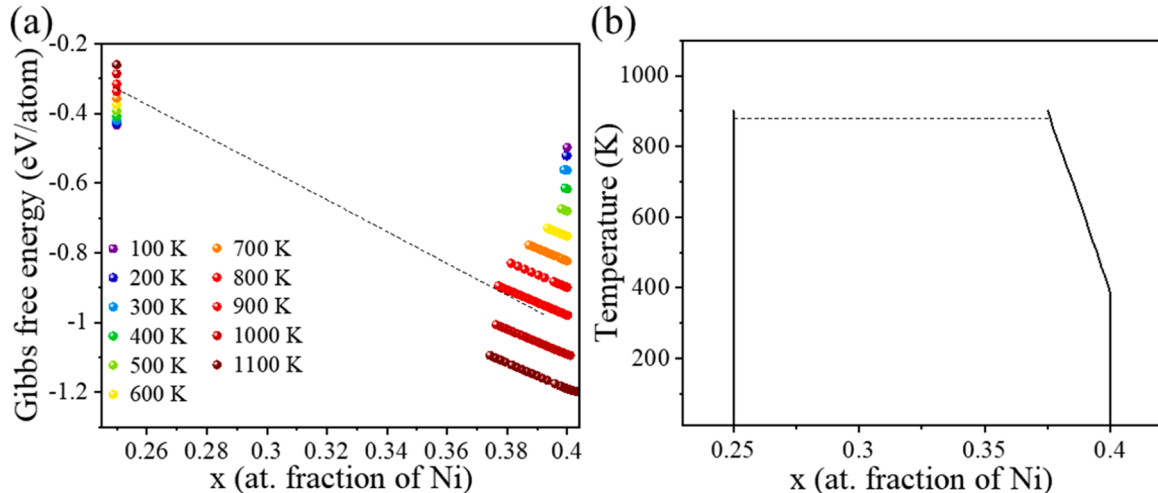
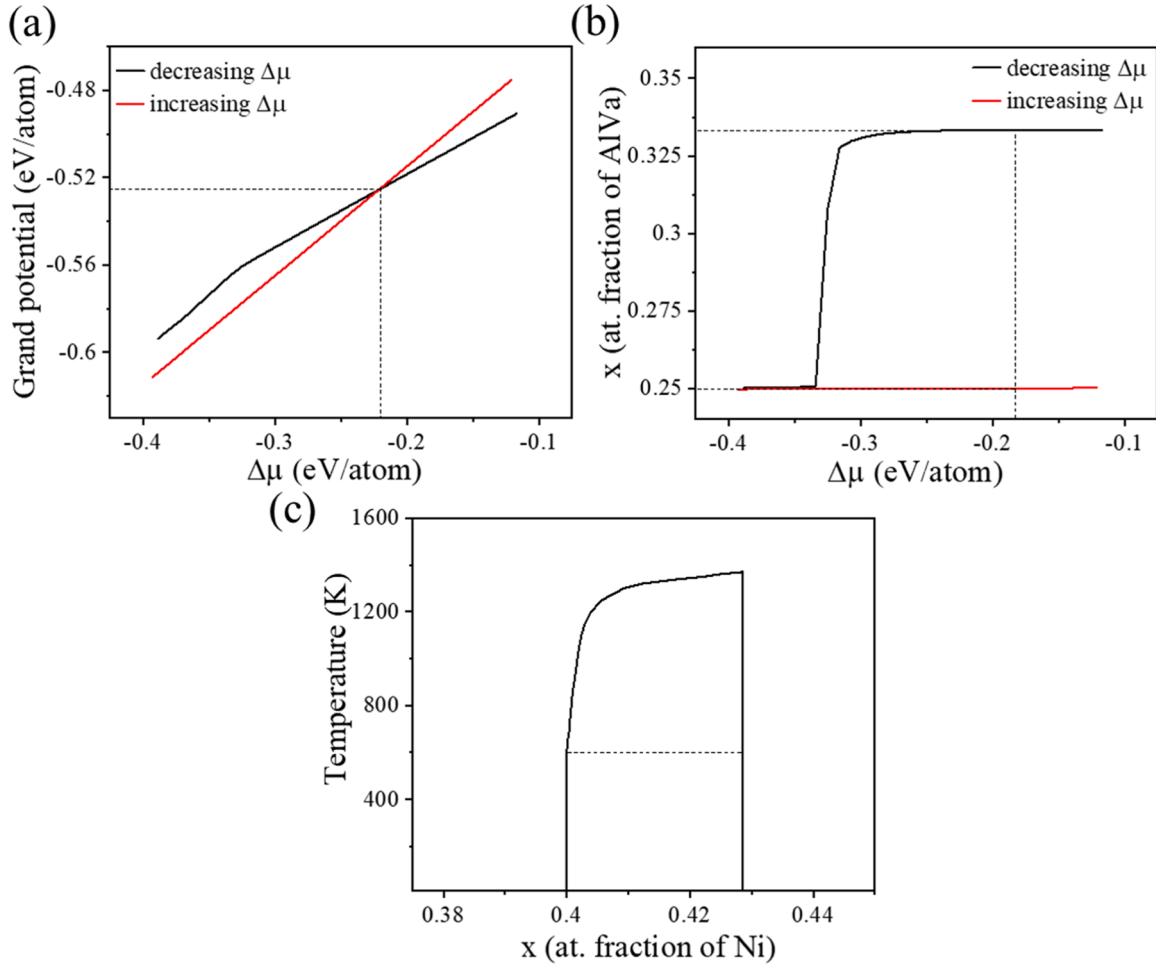


Fig. 13. (a) Gibbs free energies of Al<sub>3</sub>Ni and Al<sub>3</sub>Ni<sub>2</sub> at different temperatures. (b) Phase boundary between Al<sub>3</sub>Ni and Al<sub>3</sub>Ni<sub>2</sub>.



**Fig. 14.** (a) Grand potentials of  $\text{Al}_3\text{Ni}_2$  and  $\text{Al}_4\text{Ni}_3$  as a function of chemical potential  $\Delta\mu$  at 600 K. (b) Composition of AlVa as a function of chemical potential at 600 K. (c) Phase boundary between  $\text{Al}_3\text{Ni}_2$  and  $\text{Al}_4\text{Ni}_3$ .

above 930 K, which means that they become solid solutions.

#### 4.2. $\text{Al}_3\text{Ni}$ - $\text{Al}_3\text{Ni}_2$ phase boundary

The other adjacent phase to  $\text{Al}_3\text{Ni}$  is  $\text{Al}_3\text{Ni}_2$  and the phase boundary between them can also be determined through the common tangent to their Gibbs free energies because both phases have different lattice structure. The Gibbs free energies of  $\text{Al}_3\text{Ni}$  and  $\text{Al}_3\text{Ni}_2$  are plotted as a function of temperature in Fig. 13(a). The dashed line represents the common tangent at 900 K. Above 900 K, the common tangent to their Gibbs free energy does not exist, indicating that they become solid solutions. According to Fig. 13(a), the two-phase region between  $\text{Al}_3\text{Ni}$  and  $\text{Al}_3\text{Ni}_2$  is drawn in Fig. 13(b).

#### 4.3. $\text{Al}_3\text{Ni}_2$ - $\text{Al}_4\text{Ni}_3$ phase boundary

$\text{Al}_3\text{Ni}_2$  and  $\text{Al}_4\text{Ni}_3$  phases are both in the bcc lattice with vacancies, and the phase boundary between them can be determined from the intersection of the grand potentials. They are plotted as a function of  $\Delta\mu$  at 600 K in Fig. 14(a). It should be noted that the conjugated of  $\Delta\mu$  in Fig. 14(b) is the composition of AlVa because of the sites accommodation in the bcc lattice with vacancies. The composition of AlVa for  $\text{Al}_3\text{Ni}_2$  is 1/3 while that of  $\text{Al}_4\text{Ni}_3$  is 0.2485713, which correspond to a Ni content of 0.4 and 0.42857, respectively. The black curves in Fig. 14(a) and (b) are obtained from  $\text{Al}_3\text{Ni}_2$  by decreasing  $\Delta\mu$ , while the red ones are obtained from  $\text{Al}_4\text{Ni}_3$  by decreasing  $\Delta\mu$ .  $\phi_{\text{Al}_4\text{Ni}_3}$  and  $\phi_{\text{Al}_3\text{Ni}_2}$  intersect in Fig. 14(a). On the left of the intersection,  $\phi_{\text{Al}_4\text{Ni}_3} < \phi_{\text{Al}_3\text{Ni}_2}$ , which

indicates that  $\text{Al}_4\text{Ni}_3$  is more stable. On the right,  $\phi_{\text{Al}_4\text{Ni}_3} > \phi_{\text{Al}_3\text{Ni}_2}$  and  $\text{Al}_3\text{Ni}_2$  is more stable. The intersection is mapped onto the conjugated composition of AlVa, which is shown in Fig. 14(b). Then, the atomic fraction of Ni in  $\text{Al}_3\text{Ni}_2$  and  $\text{Al}_4\text{Ni}_3$  can be obtained and the phase boundary between  $\text{Al}_3\text{Ni}_2$  and  $\text{Al}_4\text{Ni}_3$  at 600 K can be constructed, and it is shown by the dashed line in Fig. 14(c). In this way, the phase boundary between  $\text{Al}_3\text{Ni}_2$  and  $\text{Al}_4\text{Ni}_3$  is built. It shows that  $\text{Al}_4\text{Ni}_3$  is a line compound. Above 1370 K, the grand potentials for  $\text{Al}_3\text{Ni}_2$  and  $\text{Al}_4\text{Ni}_3$  are overlapped, indicating that they become a solid solution.

#### 4.4. $\text{Al}_4\text{Ni}_3$ -AlNi phase boundary

$\text{Al}_4\text{Ni}_3$  is also adjacent to AlNi. Even though AlNi has a bcc lattice, it can also be considered a particular bcc lattice with vacancies, in which the fraction of AlVa is equal to zero. Therefore, the phase boundary between  $\text{Al}_4\text{Ni}_3$  and AlNi can be obtained from the grand potential obtained by MC simulations in the bcc lattice with vacancies. The grand potentials at 750 K are shown Fig. 15(a). The black curve corresponds to  $\text{Al}_4\text{Ni}_3$  by decreasing  $\Delta\mu$ , while the red one is obtained from AlNi by decreasing  $\Delta\mu$ . The conjugated composition of AlVa is shown in Fig. 15(b), where the composition of AlVa for  $\text{Al}_4\text{Ni}_3$  is 0.2485713 and 0 for AlNi. The equilibrium composition of Ni in  $\text{Al}_4\text{Ni}_3$  and AlNi is determined by the intersection of both curves and the phase boundary between  $\text{Al}_4\text{Ni}_3$  and AlNi is plotted in Fig. 15(c). Above 1370 K, the grand potentials of  $\text{Al}_4\text{Ni}_3$  and AlNi are overlapped and they become a solid solution.



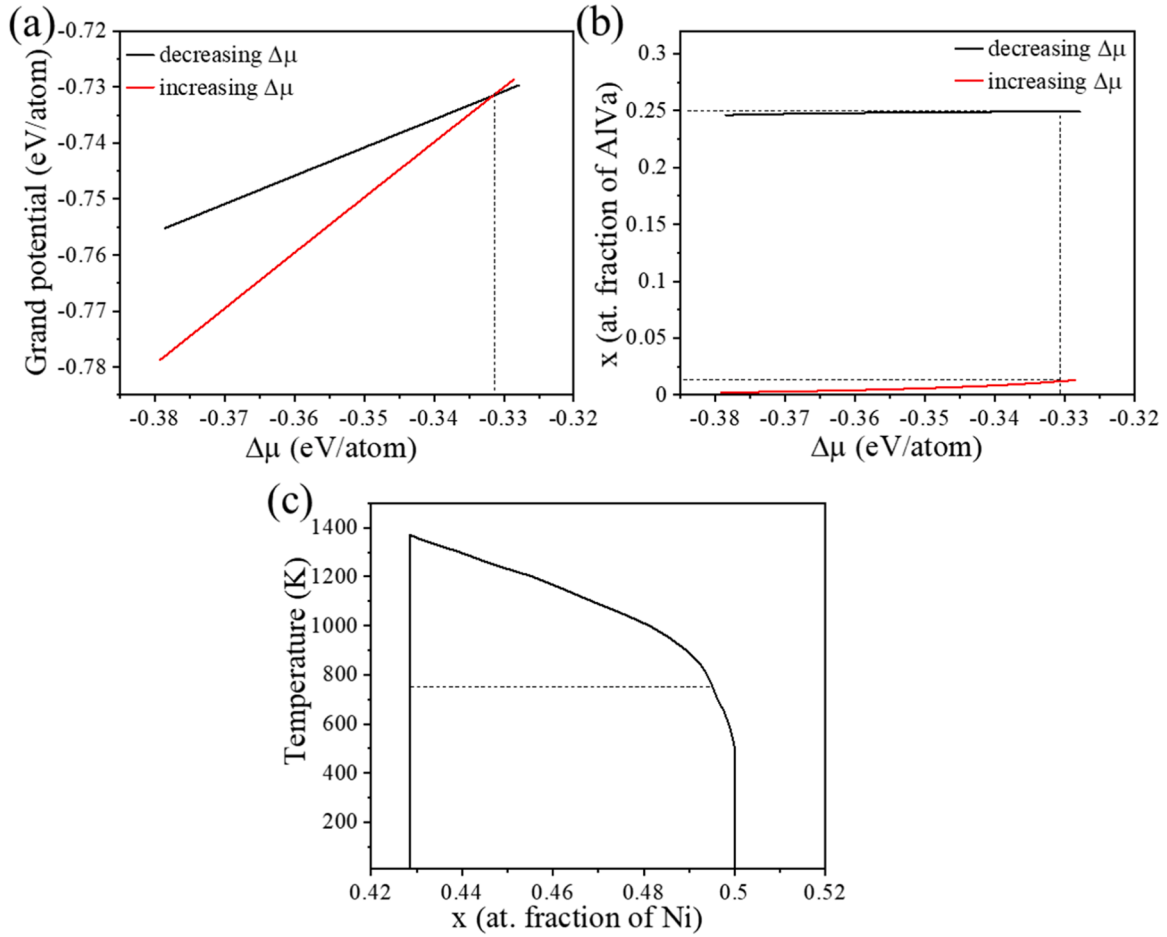


Fig. 15. (a) Grand potentials of  $\text{Al}_4\text{Ni}_3$  and  $\text{AlNi}$  as a function of the chemical potential  $\Delta\mu$  at 750 K. (b) Composition of  $\text{AlVa}$  as a function of chemical potential as a function of  $\Delta\mu$  at 750 K. (c) Phase boundary between  $\text{Al}_4\text{Ni}_3$  and  $\text{AlNi}$ .

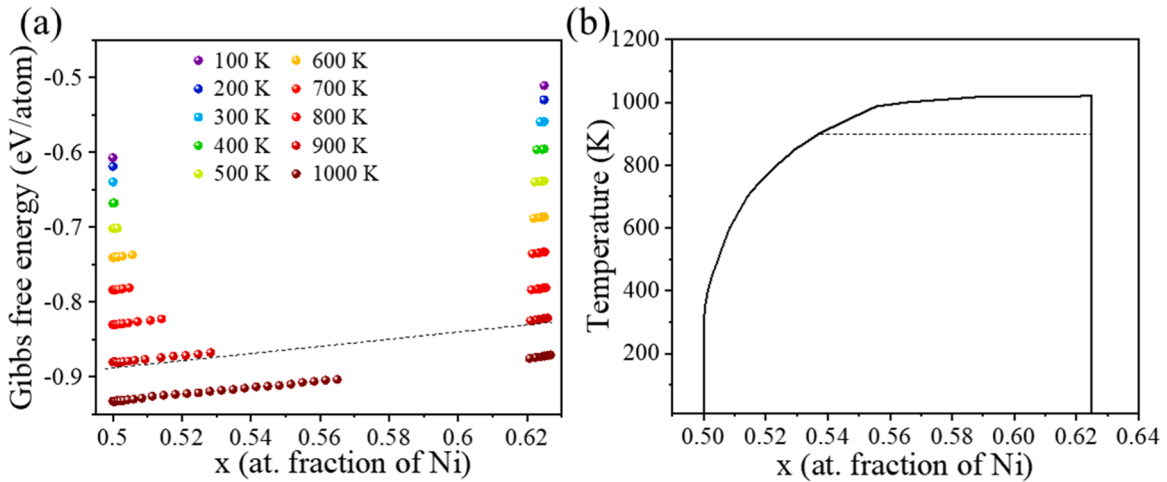
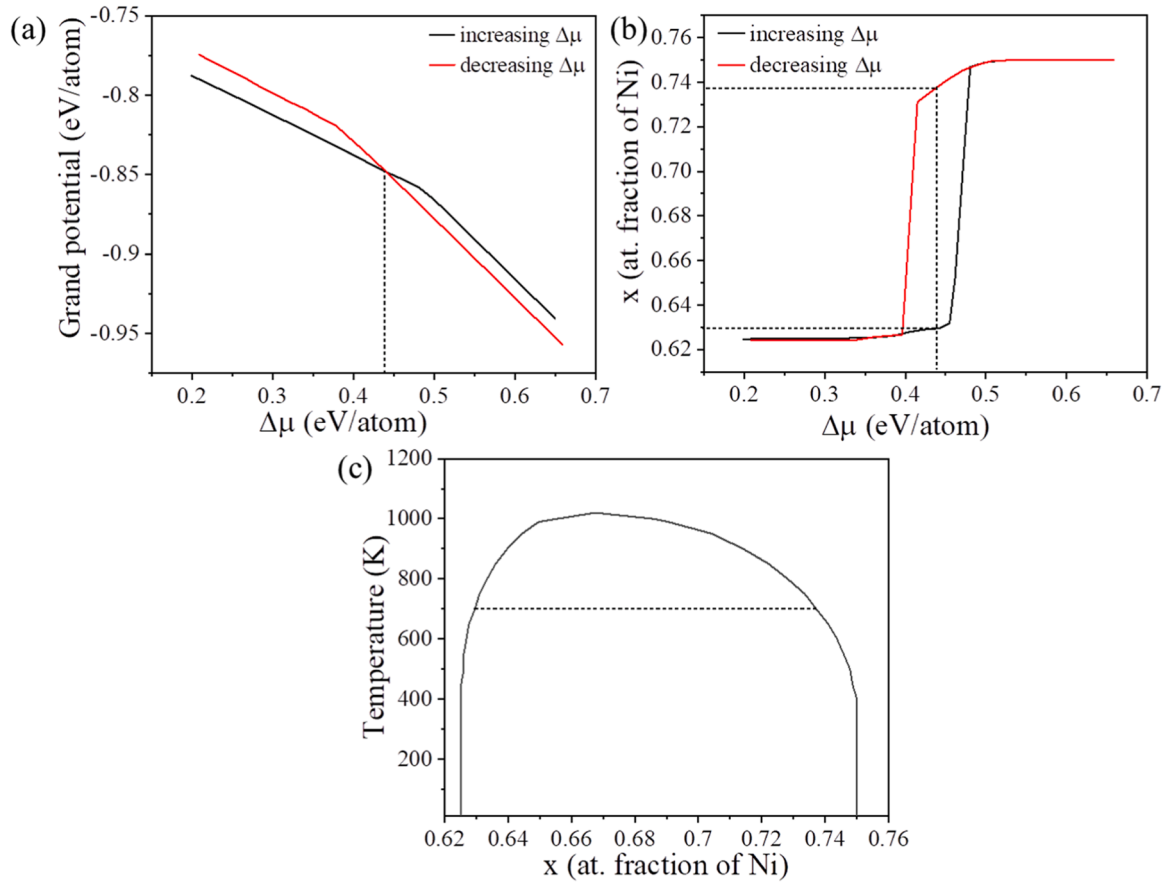


Fig. 16. (a) Gibbs free energy of  $\text{AlNi}$  and  $\text{Al}_3\text{Ni}_5$  at different temperatures. (b) Phase boundary between  $\text{AlNi}$  and  $\text{Al}_3\text{Ni}_5$ .

#### 4.5. $\text{AlNi}$ - $\text{Al}_3\text{Ni}_5$ phase boundary

The adjacent phase to  $\text{AlNi}$  on the other side of the phase diagram is  $\text{Al}_3\text{Ni}_5$ , which has a fcc lattice. Therefore, the phase boundary between  $\text{AlNi}$  and  $\text{Al}_3\text{Ni}_5$  can only be determined by the common tangent of their Gibbs free energy. The dash black line in Fig. 16(a) stands for the common tangent at 900 K, which indicates the equilibrium chemical

potential of  $\text{AlNi}$  and  $\text{Al}_3\text{Ni}_5$ . The common tangent always cuts the Gibbs free energy of  $\text{Al}_3\text{Ni}_5$  at  $x = 0.625$ , which indicates  $\text{AlNi}$  does not have any solubility in  $\text{Al}_3\text{Ni}_5$ . The two-phase region of  $\text{AlNi}$  and  $\text{Al}_3\text{Ni}_5$  exists up to 1020 K, which is slightly higher than that in experimental phase diagram (973 K) [21]. The Gibbs free energies of  $\text{AlNi}$  and  $\text{Al}_3\text{Ni}_5$  overlap with each other above 1020 K.



**Fig. 17.** (a) Grand potentials of Al<sub>3</sub>Ni<sub>5</sub> and AlNi<sub>3</sub> as a function of chemical potential at 700 K. (b) Composition of Ni as a function of chemical potential at 700 K. (c) Phase boundary between Al<sub>3</sub>Ni<sub>5</sub> and AlNi<sub>3</sub>.

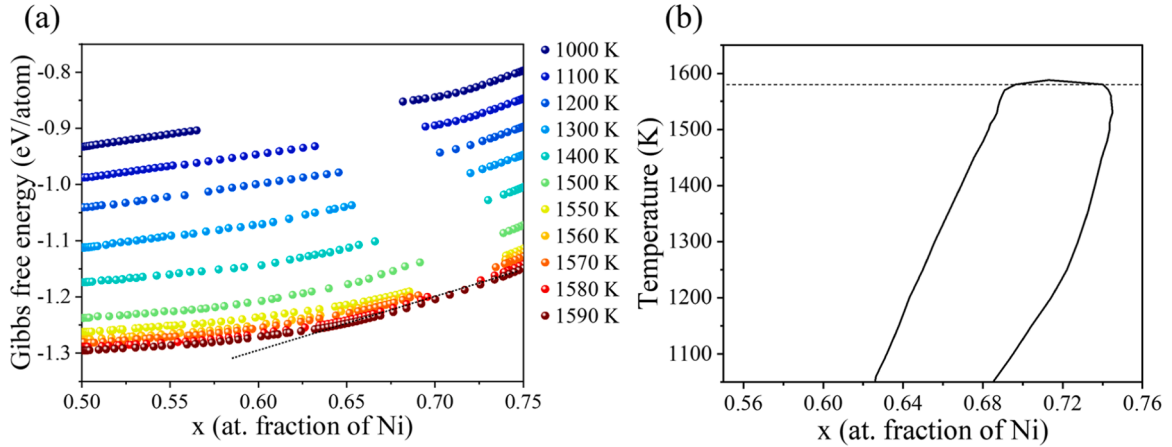


**Fig. 18.** (a) Gibbs free energy of AlNi and AlNi<sub>3</sub> at temperature above 1000 K; (b) Phase boundary between AlNi and Al<sub>3</sub>Ni<sub>5</sub>.

#### 4.6. Al<sub>3</sub>Ni<sub>5</sub>-AlNi<sub>3</sub> phase boundaries

Al<sub>3</sub>Ni<sub>5</sub> and AlNi<sub>3</sub> are both in the fcc lattice, so their phase boundary can be determined by the intersection of their grand potentials, which is shown in Fig. 17(a) at 700 K. The black curve indicates the grand potential obtained from Al<sub>3</sub>Ni<sub>5</sub> by increasing chemical potential, while the red curve indicated that obtained from AlNi<sub>3</sub> by decreasing chemical potential. The intersection is mapped onto the conjugated composition of Ni (Fig. 17(b)) and the equilibrium composition of Ni in Al<sub>3</sub>Ni<sub>5</sub> and AlNi<sub>3</sub> at 700 K was determined. The phase boundary between Al<sub>3</sub>Ni<sub>5</sub> and AlNi<sub>3</sub> is plotted in Fig. 17(c).

#### 4.7. AlNi-AlNi<sub>3</sub> phase boundary

According to literature, the two-phase region between AlNi and AlNi<sub>3</sub> was observed at high temperature. Therefore, the phase boundary between them was constructed according to the common tangent of their Gibbs free energy. The result is shown in Fig. 18. Above 1550 K, the Gibbs free energy of both phases are gradually approaching, and the two phase region (whose boundaries are indicated by the difference in composition of the intersection of the common tangent with both free energy curves) shrinks. It is in between  $x = 0.690$  for AlNi and  $x = 0.744$  for AlNi<sub>3</sub> at 1560 K and  $x = 0.696$  for AlNi and  $x = 0.738$  for AlNi<sub>3</sub> at

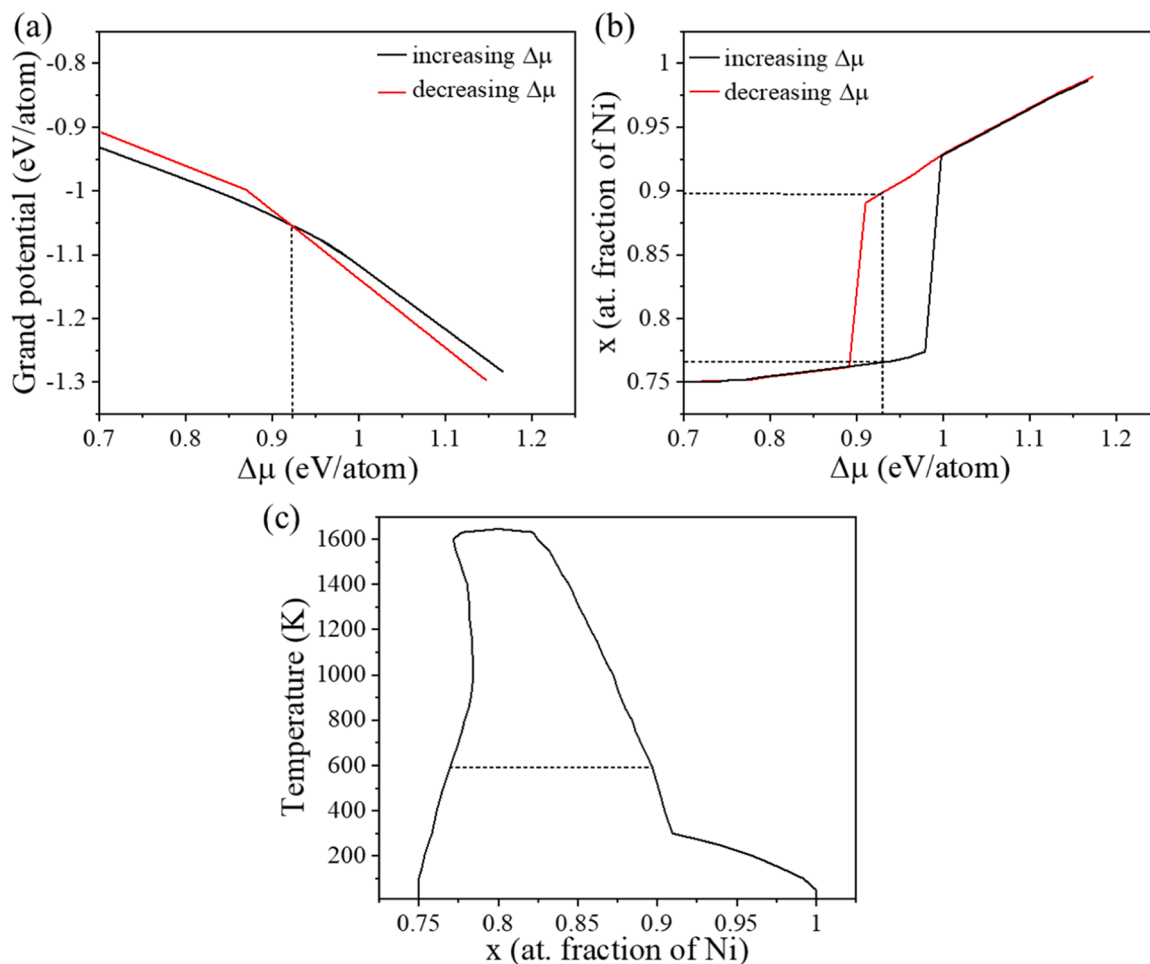


**Fig. 19.** (a) Grand potentials of  $\text{AlNi}_3$  and Ni as a function of chemical potential at 600 K. (b) Composition of Ni as a function of chemical potential at 600 K. (c) Phase boundary between  $\text{AlNi}_3$  and Ni.

1570 K. Finally, the Gibbs free energies of both phases become a continuous curve at 1590 K and the two phase region disappears, leading to a rounded top of two-phase boundary.

#### 4.8. $\text{AlNi}_3$ –Ni phase boundary

Finally, the intersection of the grand potential was used to obtain the phase boundary between  $\text{AlNi}_3$  and Ni, since both share the fcc lattice. The grand potentials obtained by increasing and decreasing chemical potential at 600 K are plotted in Fig. 19(a) and the conjugated composition of Ni is plotted in Fig. 19(b), from which the phase boundary between  $\text{AlNi}_3$  and Ni is obtained (Fig. 19(c)). The two-phase region between  $\text{AlNi}_3$  and Ni exists up to 1640 K, which is slightly higher than that in experimental phase diagram (1623 K) [13].

### 5. Discussion

#### 5.1. Comparison with the experimental phase diagram

The phase boundaries between adjacent phases were integrated to build the Ni–Al phase diagram, which is plotted in Fig. 20(a) with red lines. The black lines in Fig. 20 stand for the accepted experimental phase diagram [13]. Overall, the calculated phase diagram is in excellent agreement with the experimental one, and this result demonstrates the potential of this methodology to determine the thermodynamic properties of each phase by including configurational and vibrational entropic contributions as well as the magnetic enthalpy. The calculated

Al– $\text{Al}_3\text{Ni}$  two-phase region and the  $\text{Al}_3\text{Ni}$ – $\text{Al}_3\text{Ni}_2$  two-phase regions are practically superposed to the experimental ones up to 900 K. The solubility of Ni in  $\alpha$ -Al matrix is very low: simulations predicted a maximum solubility of 3.5 at.% at 930 K while the experimental phase diagram reaches 4.5 at.% at 916 K. The  $\text{Al}_3\text{Ni}$  phase is a line compound with a critical equilibrium temperature of 930 K according to our calculations, which is very close to 916 K in the experimental phase diagram. Moreover, the phase boundaries of the  $\text{Al}_4\text{Ni}_3$  phase in the Al-rich region of the phase diagram were determined. This line compound with a critical equilibrium temperature of 1370 K was recently reported experimentally [15,77].

An  $\text{AlNi}$  single-phase region appears in the phase diagram at high temperature, which is facilitated by different mechanisms, namely vacancies on the Ni sublattice in the Al-rich part and the substitution of Al atoms by Ni atoms on the Al sublattice in the Ni-rich part. The right boundary of the  $\text{AlNi}$  single-phase region (which is also the left boundary of the  $\text{AlNi}$ – $\text{Al}_3\text{Ni}_5$  two-phase region) is not fully consistent with the experimental one. The discrepancy can be attributed transformation mechanism responsible for the nucleation of  $\text{Al}_3\text{Ni}_5$ .  $\text{Al}_3\text{Ni}_5$  is an intermediate product of the reversible martensitic transformation from  $\text{B}_2$  to  $\text{L}_{10}$  and the presence and composition of  $\text{Al}_3\text{Ni}_5$  is controlled by the aging temperature and the heating rate. For instance, the  $\text{Al}_3\text{Ni}_5$  phase may come directly from the  $\text{L}_{10}$  martensite during a heating-up stage if the heating rate was not fast enough [73]. The  $\text{Al}_3\text{Ni}_5$  phase can also be formed from  $\text{B}_2$  after aging at 500 °C [23]. Different formation mechanisms may lead to large discrepancies in the experimental left boundary of the  $\text{AlNi}$ – $\text{Al}_3\text{Ni}_5$  two-phase region boundary and the

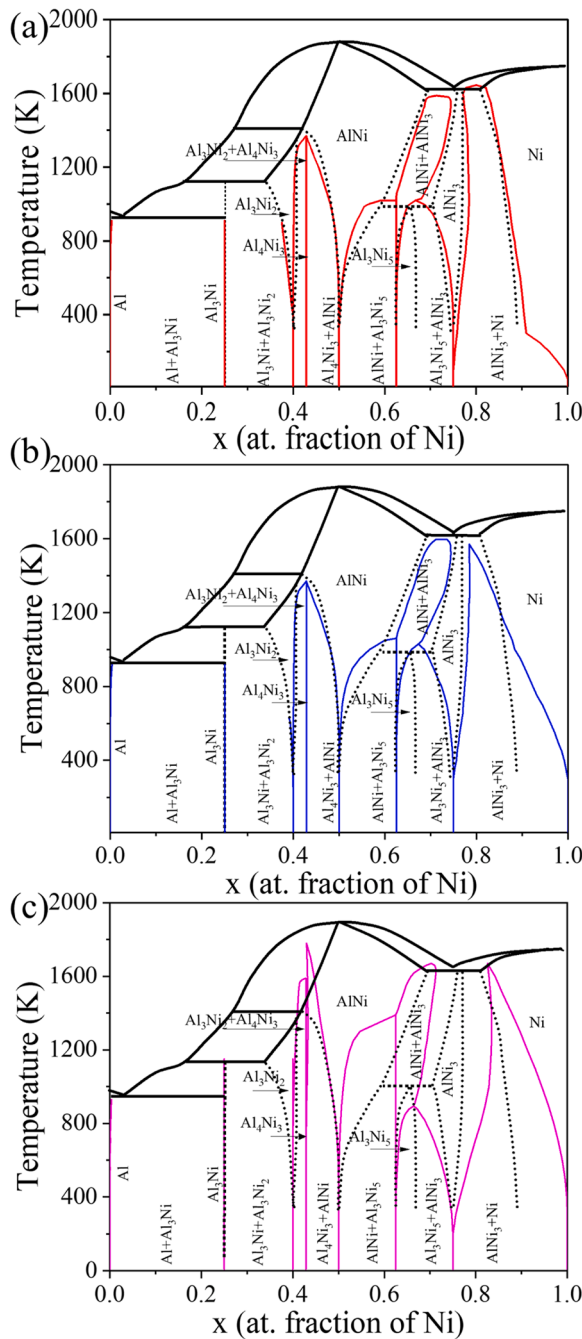


**Fig. 20.** Comparison of the solid-state region of the experimental NiAl phase diagram [13] (dashed black lines) with those obtained for first principles calculations. (a) Calculated phase diagram including magnetic enthalpy as well as configurational and vibrational entropy (red lines). (b) Calculated phase diagram including only configurational and vibrational entropy (blue lines) and neglecting the magnetic enthalpy (c) Calculated phase diagram including only configurational entropy (purple lines). The thick continuous black lines stand for solidus and liquidus lines that cannot be predicted with the methodology used in this investigation.

$\text{Al}_3\text{Ni}_5$  phase was not even observed in some experiments [78]. In our calculation,  $\text{Al}_3\text{Ni}_5$  is formed from either fcc ordering or bcc ordering (the former one is more likely) by atomic diffusion and shear transformation, as explained in Section 3.1. The calculated maximum temperature for the two phase  $\text{AlNi}-\text{Al}_3\text{Ni}_5$  region is 1020 K, close to the experimental value of 973 K. Approaching the Ni-rich part, the calculated critical equilibrium temperature of  $\text{AlNi}_3$  phase (1640 K) as well as

**Table 2**

Energy difference ( $\Delta E$ ) between non-magnetic and ferromagnetic phases, magnetic moment and volume of ferromagnetic and non-magnetic  $\text{AlNi}_3$  and Ni.

Composition	$\Delta E$ (eV/atom)	Volume/atom ( $\text{\AA}^3$ )	Magnetic moment ( $\mu_B$ ) This work	Magnetic moment ( $\mu_B$ ) Experimental Calculated
Ferromagnetic $\text{AlNi}_3$	0	10.896	0.76	0.71 [79]
Non-magnetic $\text{AlNi}_3$	0.004	10.883	–	0.73 [80]
Ferromagnetic Ni	0	10.369	0.6	0.605 [81]
Non-magnetic Ni	0.061	10.312	–	0.65 [82]

the solvus line are in good agreement with the experimental data. It should be noted that the calculated phase diagram provides novel information about the solvus line below 300 K. This information is not available experimentally.

## 5.2. Influence of magnetism and vibrational entropy

One advantage of the simulations is that the different contributions to the thermodynamic properties of the phases can be turned off to ascertain their influence. Thus, the Ni-Al phase diagram can be obtained following exactly the same methodology but neglecting the effect of magnetic enthalpy. This is achieved by assuming that the stable phase reference phases in the Ni-rich part of the Ni-Al phase diagram ( $\gamma$ -Ni and  $\gamma'$ - $\text{AlNi}_3$ ) are non-magnetic. The Energy difference ( $\Delta E$ ), magnetism moment and volume of ferromagnetic and non-magnetic  $\text{AlNi}_3$  and Ni are compared in Table 2. The total magnetic moments of the ferromagnetic phases are in a good agreement with experimental and calculated data in the literature references. Moreover, the total energy of ferromagnetic Ni slightly lower than that of non-magnetic Ni (the energy difference between them is in Table 2) indicating that the former is more stable. The differences in the total energy between ferromagnetic and non-magnetic  $\text{AlNi}_3$  are, however, negligible. Therefore, neglecting the magnetic contribution can lead to important errors in the calculation of the Ni-rich region of the phase diagram. The whole solid phase diagram was built without considering the magnetic enthalpy and it is plotted in Fig. 20(b). The corresponding phase boundaries between adjacent phases are depicted in Section SI in the supplementary material. As expected, the calculated  $\text{AlNi}_3$ -Ni boundary in the phase diagram show large discrepancies with the experimental one. It should be noted that the spins will fluctuate at higher temperature, leading to an entropic magnetic contribution from magnetism. This contribution is smaller than the configurational and vibrational ones and it was ignored in this work.

The predicted Ni-Al phase diagram only considering the configurational entropic contribution is shown by the green lines in Fig. 20(c). The corresponding phase boundaries between adjacent phases are depicted in Section SII in the supplementary material. Overall, the phase diagram at low temperatures is very similar to the one in Fig. 2(a) because the configurational enthalpy (namely the formation energy) dominates over the entropic contributions. Nevertheless, large discrepancies arise in the critical equilibrium temperatures. For instance, the maximum temperature of  $\text{Al}_3\text{Ni}_2$ - $\text{Al}_4\text{Ni}_3$ ,  $\text{Al}_4\text{Ni}_3$ - $\text{AlNi}$  and  $\text{AlNi}$ - $\text{Al}_3\text{Ni}_5$  two phase regions are overestimated by several hundred K, while the  $\text{Al}_3\text{Ni}_5$ - $\text{AlNi}_3$  two phase region is several hundred K below the experimental one. The solubility of phases is also affected by the vibrational entropic contribution, especially in the Ni-rich part. Therefore, the formation enthalpy can provide the information about the stoichiometry and the lattice of stable phases, while the addition of the configurational entropy allows good enough predictions of the low temperature region of the phase diagram. However, the lattice vibration contribution has to be taken into account if accuracy is needed at high temperature.



## 6. Conclusions

The solid-state region of the Ni-Al phase diagram was predicted by means of first principle simulations and statistical mechanics. It was found that all phases – with the exception of  $\text{Al}_3\text{Ni}$  – can be treated as configurations existing on fcc or bcc lattices, with the atomic sites accommodating Al and Ni atoms, or – in the case of  $\text{Al}_3\text{Ni}_2$  – bcc lattices with the Ni sublattice sites of AlNi accommodating Ni atoms and vacancies. The temperature-dependent mixing enthalpies of the configurations in each lattice were approximated by the cluster expansion formalism, including the effect of magnetism and of vibrational entropy which was calculated from the corresponding length-stiffness relationships. The thermodynamic grand potential of each phase and the Gibbs free energy were calculated from Monte Carlo simulations and used to predict the phase diagram.

Seven ground state phases were found at 0 K, namely Al,  $\text{Al}_3\text{Ni}$ ,  $\text{Al}_3\text{Ni}_2$ ,  $\text{Al}_4\text{Ni}_3$ , AlNi,  $\text{Al}_3\text{Ni}_5$ ,  $\text{AlNi}_3$  and Ni. Among them,  $\text{Al}_4\text{Ni}_3$  and  $\text{Al}_3\text{Ni}$  were line compounds. The predicted phase diagram was in excellent agreement with the current experimentally accepted Al-Ni phase diagram and provided accurate predictions of the two-phase boundaries, critical equilibrium temperatures and solubility of the phases. Overall, these results demonstrate the accuracy of the methodology employed to predict accurately the phase diagram of alloys of technological interest. Moreover, the accurate values of the free energies of the different phases can be confidently extrapolated to predict the phase diagrams of more complex systems based on Ni-Al.

Predictions of the phase diagram were also carried out neglecting the effect of magnetism and of vibrational entropy. They showed that the former is important to predict the phase boundaries and the critical equilibrium temperatures in the Ni-rich of the phase diagram (> 75% Ni) while vibrational entropy is necessary to predict accurately the features of the phase diagram (two phase boundaries, solubilities, critical equilibrium temperatures) above 400 K.

## Data availability

The computational data generated in this investigation can be obtained upon request to the corresponding author.

## Declaration of Competing Interest

The authors declare that they do not have conflicts of interest to disclose.

## Acknowledgements

This investigation was supported by the European Union's Horizon 2020 research and innovation program through a Marie Skłodowska-Curie Individual Fellowship (Grant Agreement 893883) and also by the project (MAD2D-CM)-IMDEA Materials funded by Comunidad de Madrid, by the Recovery, Transformation and Resilience Plan, and by NextGenerationEU from the European Union, as well as by the Innovation Ability Promotion Program of Hebei (22567609H). Additional support from the Comunidad de Madrid under the Multiannual Agreement with UC3M in the line of Excellence of University Professors (EPUC3M23), in the context of the 5th PRICIT is also acknowledged. Computer resources and technical assistance provided by the Centro de Supercomputación y Visualización de Madrid (CeSViMa) and by the Spanish Supercomputing Network (project FI-2021-3-6) are gratefully acknowledged. Wei Shao also acknowledges the support from the China Scholarship Council.

## Supplementary materials

Supplementary material associated with this article can be found, in the online version, at [doi:10.1016/j.actamat.2023.118962](https://doi.org/10.1016/j.actamat.2023.118962).

## References

- [1] R. Novakovic, M. Mohr, D. Giuranno, E. Ricci, J. Brillo, R. Wunderlich, I. Egry, Y. Plevchuk, H.-J. Fecht, Surface properties of liquid Al-Ni Alloys: experiments Vs theory, *Micrograv. Sci. Technol.* 32 (2020) 1049–1064.
- [2] J. Wen, H.Z. Cui, N. Wei, X.J. Song, G.S. Zhang, C.M. Wang, Q. Song, Effect of phase composition and microstructure on the corrosion resistance of Ni-Al intermetallic compounds, *J. Alloys Compd.* 695 (2017) 2424–2433.
- [3] J. Llorca, P. Poza, Fracture toughness of Al/SiC composites in the temperature range -136 °C to 190 °C, *Scripta Metallurgica et Materialia; (United States)* 29 (2) (1993).
- [4] A. Martín, M.A. Martínez, J. Llorca, Wear of SiC-reinforced Al-matrix composites in the temperature range 20–200 °C, *Wear* 193 (1996) 169–179.
- [5] A.A.S. Akl, M. Elhadi, Estimation of crystallite size, lattice parameter, internal strain and crystal impurification of nanocrystalline  $\text{Al}_3\text{Ni}_{20}\text{B}_x$  alloy by williamson-hall method, *J. Ovonic Res.* 16 (2020) 323–335.
- [6] A.-P. Tsai, A. Inoue, T. Masumoto, Ductile Al-Ni-Zr amorphous alloys with high mechanical strength, *J. Mater. Sci. Lett.* 7 (1988) 805–807.
- [7] M.I. Flores-Zamora, C.A. Martínez-Pérez, M. García-Guaderrama, I. Estrada-Guel, F. Espinosa-Maga, Comparative study of Al-Ni-Mo alloys obtained by mechanical alloying in different ball mills, *Rev. Adv. Mater. Sci.* 18 (2008) 301–304.
- [8] C.T. Liu, V.K. Sikka, Nickel aluminides for structural use, *JOM* 38 (1986) 19–21.
- [9] M.L. Bakker, D.J. Young, M.S. Wainwright, Selective leaching of  $\text{NiAl}_3$  and  $\text{Ni}_2\text{Al}_3$  intermetallics to form Raney nickels, *J. Mater. Sci.* 23 (1988) 3921–3926.
- [10] Y.-J. Lee, Y.-S. Lee, J.Y. Cha, Y.S. Jo, H. Jeong, H. Sohn, C.W. Yoon, Y. Kim, K.-B. Kim, S.W. Nam, Development of porous nickel catalysts by low-temperature Ni-Al chemical alloying and post selective Al leaching, and their application for ammonia decomposition, *Int. J. Hydrog. Energy* 45 (2020) 19181–19191.
- [11] W.R. Osório, L.C. Peixoto, M.V. Canté, A. García, Electrochemical corrosion characterization of Al-Ni alloys in a dilute sodium chloride solution, *Electrochim. Acta* 55 (2010) 4078–4085.
- [12] I. Ansara, B. Sundman, P. Willemin, Thermodynamic modeling of ordered phase in the Ni-Al system, *Acta Metall* 36 (1988) 977–982.
- [13] Y. Du, N. Clavaguera, Thermodynamic assessment of the Al-Ni system, *J. Alloys Compd.* 237 (1996) 20–32.
- [14] W. Huang, Y.A. Chang, A thermodynamic analysis of the Ni-Al system, *Intermetallics* 6 (1998) 487–498.
- [15] W. Yang, P. Wang, X. Huang, S. Zhang, Thermodynamic analysis of the Al-Ni system, *Intermetallics* 149 (2022), 107647.
- [16] M. Hillert, The compound energy formalism, *J. Alloys Compd.* 320 (2001) 161–176.
- [17] M. Yasseri, A. Sankhla, H. Kamila, R. Orenstein, D.Y.N. Truong, N. Farahi, J. de Boor, E. Mueller, Solid solution formation in  $\text{Mg}_2(\text{Si}, \text{Sn})$  and shape of the miscibility gap, *Acta Mater* 185 (2020) 80–88.
- [18] C. Nataraj, E.J.L. Borda, A. van de Walle, A. Samanta, A systematic analysis of phase stability in refractory high entropy alloys utilizing linear and non-linear cluster expansion models, *Acta Mater* 220 (2021), 117269.
- [19] Y.Z. Zhan, Y. Du, Y.H. Zhuang, Chapter four-determination of phase diagrams using equilibrated alloys, in: J.-C. Zhao (Ed.), *Methods For Phase Diagram Determination*, Elsevier Science Ltd, Oxford, 2007, pp. 108–150.
- [20] S. Tsuji, Numerical modeling of multiphase diffusion in the process of homogenizing in binary alloys, *Metall. Mater. Trans. A* 32 (2001) 681–690.
- [21] I.M. Robertson, C.M. Wayman,  $\text{Ni}_5\text{Al}_3$  and the nickel-aluminum binary phase diagram, *Metallogr* 17 (1984) 43–55.
- [22] D. Schryvers, L. Toth, Y. Ma, L. Tanner, Nucleation and Growth of the  $\text{Ni}_5\text{Al}_3$  Phase in Ni-Al Austenite and Martensite, *J. Phys. IV France* 05 (1995) C2-299-C2-304.
- [23] P.S. Khadkikar, K. Vedula, An investigation of the  $\text{Ni}_5\text{Al}_3$  phase, *J. Mater. Res.* 2 (1987) 163–167.
- [24] D. Schryvers, Y. Ma, The growth of  $\text{Ni}_5\text{Al}_3$  in  $\text{Ll}_0$  martensite studied by in situ transmission electron microscopy and high resolution electron microscopy, *J. Alloys Compd.* 221 (1995) 227–234.
- [25] C.F. Li, Y.P. Ren, G.W. Qin, Experimental confirmation of  $\text{Ni}_5\text{Al}_3$  Phase in Ni-Al binary system by diffusion couple technique, *AMR* 299–300 (2011) 224–227.
- [26] K. Bochenek, M. Basista, Advances in processing of NiAl intermetallic alloys and composites for high temperature aerospace applications, *Prog. Aerosp. Sci.* 79 (2015) 136–146.
- [27] J.H. Yang, C.M. Wayman, On the formation mechanism of  $\text{Ni}_5\text{Al}_3$  in NiAl-base alloys: part I. Microstructures, *Intermetallics* 2 (1994) 111–119.
- [28] C. Ravi, H.K. Sahu, M.C. Valsakumar, A. van de Walle, Cluster expansion Monte Carlo study of phase stability of vanadium nitrides, *Phys. Rev. B* 81 (2010), 104111.
- [29] S. Liu, E. Martínez, J. Llorca, Prediction of the Al-rich part of the Al-Cu phase diagram using cluster expansion and statistical mechanics, *Acta Mater* 195 (2020) 317–326.
- [30] D. Cheng, K. Wang, B.-C. Zhou, Crystal structure and stability of phases in Mg-Zn alloys: a comprehensive first-principles study, *Acta Mater.* 242 (2023), 118443.
- [31] K. Li, C.-C. Fu, Ground-state properties and lattice-vibration effects of disordered Fe-Ni systems for phase stability predictions, *Phys. Rev. Mater.* 4 (2020), 023606.
- [32] J.M. Sanchez, J.P. Stark, V.L. Moruzzi, First-principles calculation of the Ag-Cu phase diagram, *Phys. Rev. B* 44 (1991) 5411–5418.
- [33] R. Arroyave, D. Shin, Z.-K. Liu, Ab initio thermodynamic properties of stoichiometric phases in the Ni-Al system, *Acta Mater* 53 (2005) 1809–1819.
- [34] L. Monacelli, R. Bianco, M. Cherubini, M. Calandra, I. Errea, F. Mauri, The stochastic self-consistent harmonic approximation: calculating vibrational properties of materials with full quantum and anharmonic effects, *J. Phys.: Condens. Matter* 33 (2021), 363001.

- [35] A. Togo, I. Tanaka, First principles phonon calculations in materials science, *Scripta Mater* 108 (2015) 1–5.
- [36] T. Kameccek, S. Wieser, H. Kojima, N. Bedoya-Martínez, J.P. Dürholt, R. Schmid, E. Zojer, Evaluating computational shortcuts in supercell-based phonon calculations of molecular crystals: the instructive case of naphthalene, *J. Chem. Theory Comput.* 16 (2020) 2716–2735.
- [37] F. Geng, J.R. Boes, J.R. Kitchin, First-principles study of the Cu-Pd phase diagram, *Calphad* 56 (2017) 224–229.
- [38] H. Tao Xue, F.L. Tang, X. Kang Li, F. Cheng Wan, W. Jiang Lu, Z. Yuan Rui, Y. Dong Feng, Phase equilibrium of a  $\text{CuInSe}_2$ – $\text{CuInS}_2$  pseudobinary system studied by combined first-principles calculations and cluster expansion Monte Carlo simulations, *Mat. Sci. Semicon. Proc.* 25 (2014) 251–257.
- [39] A. Wozniakowski, J. Deniszczyk, Phase diagram calculations for the ZnSe-BeSe system by first-principles base thermodynamic Monte Carlo integration, *Comput. Methods Mater. Sci.* 13 (2013) 351–356.
- [40] W. Shao, S. Liu, J. Llorca, First principles prediction of the Al-Li phase diagram including configurational and vibrational entropic contributions, *Comput. Mater. Sci.* 217 (2023), 111898.
- [41] A. Pasturel, C. Colinet, A.T. Paxton, M. van Schilfgaarde, First-principles determination of the Ni-Al phase diagram, *J. Phys.: Condens. Matter.* 4 (1992) 945.
- [42] J.G. Giori, A. Van der Ven, Phase and structural stability in Ni-Al systems from first principles, *Phys. Rev. B.* 94 (2016), 094111.
- [43] G.Y. Guo, Y.K. Wang, L.-S. Hsu, First-principles and experimental studies of the electronic structures and magnetism in and  $\text{Ni}_3\text{In}$ , *J. Magn. Magn. Mater.* 239 (2002) 91–93.
- [44] I. Ansara, N. Dupin, H.L. Lukas, B. Sundman, Thermodynamic assessment of the Al-Ni system, *J. Alloys Compd* 247 (1997) 20–30.
- [45] M. Fedorov, J.S. Wróbel, A. Fernández-Caballero, K.J. Kurzydowski, D. Nguyen-Manh, Phase stability and magnetic properties in fcc Fe-Cr-Mn-Ni alloys from first-principles modeling, *Phys. Rev. B.* 101 (2020), 174416.
- [46] D. Ma, B. Grabowski, F. Körmann, J. Neugebauer, D. Raabe, Ab initio thermodynamics of the  $\text{CoCrFeMnNi}$  high entropy alloy: importance of entropy contributions beyond the configurational one, *Acta Mater* 100 (2015) 90–97.
- [47] A. van de Walle, M. Asta, G. Ceder, The alloy theoretic automated toolkit: a user guide, *Calphad* 26 (2002) 539–553.
- [48] J. Paier, R. Hirschl, M. Marsman, G. Kresse, The Perdew–Burke–Ernzerhof exchange-correlation functional applied to the G2-1 test set using a plane-wave basis set, *J. Chem. Phys.* 122 (2005), 234102.
- [49] S. Scandolo, P. Giannozzi, C. Cavazzoni, S. de Gironcoli, A. Pasquarello, S. Baroni, First-principles codes for computational crystallography in the quantum-ESPRESSO package, *Z. Kristallogr. Cryst. Mater.* 220 (2005) 574.
- [50] P. Wisena, K.A. McGill, T. Mueller, Efficient generation of generalized Monkhorst-Pack grids through the use of informatics, *Phys. Rev. B.* 93 (2016), 155109.
- [51] A. van de Walle, G. Ceder, The effect of lattice vibrations on substitutional alloy thermodynamics, *Rev. Mod. Phys.* 74 (2002) 11–45.
- [52] E.J. Wu, G. Ceder, Using bond-length-dependent transferable force constants to predict vibrational entropies in Au-Cu, Au-Pd, and Cu-Pd alloys, *Phys. Rev. B* 67 (2003), 134103.
- [53] J.Z. Liu, G. Ghosh, A. van de Walle, M. Asta, Transferable force-constant modeling of vibrational thermodynamic properties in fcc-based Al–TM (TM=Ti, Zr, Hf) alloys, *Phys. Rev. B* 75 (2007), 104117.
- [54] Y.Y.F. Liu, B. Andrews, G.J. Conduit, Direct evaluation of the force constant matrix in quantum Monte Carlo, *J. Chem. Phys.* 150 (2019), 034104.
- [55] K.-P. Bohnen, R. Heid, B. Renker, Phonon dispersion and electron-phonon coupling in  $\text{MgB}_2$  and  $\text{AlB}_2$ , *Phys. Rev. Lett.* 86 (2001) 5771–5774.
- [56] O. Adjaoud, G. Steinle-Neumann, B.P. Burton, A. van de Walle, First-principles phase diagram calculations for the HfC–TiC, ZrC–TiC, and HfC–ZrC solid solutions, *Phys. Rev. B.* 80 (2009), 134112.
- [57] R. Chinnappan, B.K. Panigrahi, A. van de Walle, First-principles study of phase equilibrium in Ti–V, Ti–Nb, and Ti–Ta alloys, *Calphad* 54 (2016) 125–133.
- [58] A. van de Walle, G. Ceder, U. Waghmare, First-principles computation of the vibrational entropy of ordered and disordered  $\text{Ni}_3\text{Al}$ , *Phys. Rev. Lett.* 80 (1998).
- [59] S.B. Maisel, T.C. Kerscher, S. Müller, No miscibility gap in Pt–Rh binary alloys: a first-principles study, *Acta Mater* 60 (2012) 1093–1098.
- [60] N. Wang, T. Hammerschmidt, J. Rogal, R. Drautz, Accelerating spin-space sampling by auxiliary spin dynamics and temperature-dependent spin-cluster expansion, *Phys. Rev. B.* 99 (2019), 094402.
- [61] A. Redermeier, E. Kozeschni, Monte Carlo study of Cu precipitation in bcc-Fe: temperature-dependent cluster expansion versus local chemical environment potentials, *Model. Simul. Mater. Sci. Eng.* 29 (2021), 035014.
- [62] S. Vafaei, B. Tomberli, C.G. Gray, McMillan-mayer theory of solutions revisited: simplifications and extensions, *J. Chem. Phys.* 141 (2014), 154501.
- [63] A. van de Walle, M. Asta, Self-driven lattice-model Monte Carlo simulations of alloy thermodynamic properties and phase diagrams, *Model. Simul. Mater. Sci. Eng.* 10 (2002) 521–538.
- [64] A.I. Rusanov, A.K. Shchekin, D.V. Tatyankin, Grand potential in thermodynamics of solid bodies and surfaces, *J. Chem. Phys.* 131 (2009), 161104.
- [65] K. Wang, D. Cheng, C.-L. Fu, B.-C. Zhou, First-principles investigation of the phase stability and early stages of precipitation in Mg–Sn alloys, *Phys. Rev. Mater.* 4 (2020), 013606.
- [66] A. van de Walle, Multicomponent multisublattice alloys, nonconfigurational entropy and other additions to the alloy theoretic automated toolkit, *Calphad* 33 (2009) 266–278.
- [67] S. Liu, J. Wróbel, J. Llorca, First principles analysis of the Al-rich corner of Al–Li–Cu phase diagram, *Acta Mater* 236 (2022), 118129.
- [68] M. Ellner, S. Kek, B. Predel,  $\text{Ni}_4\text{Al}_3$  - A phase with ordered vacancies isotypic to  $\text{Ni}_3\text{Ga}_4$ , *J. less-Common. Met.* 154 (1989) 207–215.
- [69] P. Delavignette, H. Richel, S. Amelinckx, The ordering of vacancies in  $\text{Ni}_{1-x}\text{Al}$ , *Phys. Stat.* 13 (1972) 545.
- [70] T.V. Panova, V.C. Kovvichak, V.I. Blinov, X-ray diffraction analysis of double-layer systems irradiated by a high-power ion beam, *J. Surf. Investig.-X-Ra.* 2 (2008) 652–656.
- [71] J.H. Yang, C.M. Wayman, On the formation mechanism of  $\text{Ni}_5\text{Al}_3$  in NiAl-based alloys: part II, Kinetics, *Intermetallics* 2 (1994) 121–126.
- [72] M.H. Yang, Z. Zhang, Z.S. Han, J.F. Du, J.K. Huang, The formation of  $\text{Ni}_5\text{Al}_3$  phase and its effect on the mechanical properties of In783 alloy, *Intermetallics* 126 (2020), 106930.
- [73] P.L. Potapov, V.A. Udovenko, S.Y. Song, S.D. Prokoshkin, X-ray study of phase transformations in martensitic Ni–Al alloys, *Metall. Mater. Trans. A.* 28 (1997) 1133–1142.
- [74] P. Potapov, S. Song, V. Udovenko, K. Jee, Effect of  $\text{LiO} \rightarrow \text{Ni}_5\text{Al}_3$  reordering on properties of martensitic Ni–Al Alloys, *J. Phys. IV* 07 (1997). C5-245–C5-250.
- [75] B.P. Burton, A. van de Walle, First-principles phase diagram calculations for the system NaCl–KCl: the role of excess vibrational entropy, *Chem. Geol.* 225 (2006) 222–229.
- [76] X. Chong, J.P.S. Palma, Y. Wang, S.-L. Shang, F. Drymiotis, V.A. Ravi, K.E. Star, J.-P. Fleurial, Z.-K. Liu, Thermodynamic properties of the Yb–Sb system predicted from first-principles calculations, *Acta Mater.* 217 (2021), 117169.
- [77] T. Davey, N.-D. Tran, A. Saengdeejing, Y. Chen, First-principles-only CALPHAD phase diagram of the solid aluminium-nickel (Al–Ni) system, *Calphad* 71 (2020), 102008.
- [78] X. Wang, Z. Chen, D. Dong, D. Zhu, H. Wang, Z. Wei, Study on the phase selection and debye temperature of Hyper-Peritectic Al–Ni Alloy under high pressure, *Metals (Basel)* 11 (2021) 84.
- [79] A. Aguayo, I. Mazin, D. Singh, Why  $\text{Ni}_3\text{Al}$  is an itinerant ferromagnet but  $\text{Ni}_3\text{Ga}$  is not, *Phys. Rev. Lett.* 92 (2004), 147201.
- [80] L. Ortenzi, I.I. Mazin, P. Blaha, L. Boeri, Accounting for spin fluctuations beyond local spin density approximation in the density functional theory, *Phys. Rev. B.* 86 (2012), 064437.
- [81] M.Y. Lavrentiev, J.S. Wróbel, D. Nguyen-Manh, S.L. Dudarev, M.G. Ganchenkova, Magnetic cluster expansion model for random and ordered magnetic face-centered cubic Fe–Ni–Cr alloys, *J. Appl. Phys.* 120 (4) (2016), 043902.
- [82] J. Kudrnovský, V. Drchal, P. Bruno, Magnetic properties of fcc Ni-based transition metal alloys, *Phys. Rev. B.* 77 (2008), 224422.